Molecular Cell

Article

Circular RNA ZNF609/*CKAP5* mRNA interaction regulates microtubule dynamics and tumorigenicity

Graphical abstract

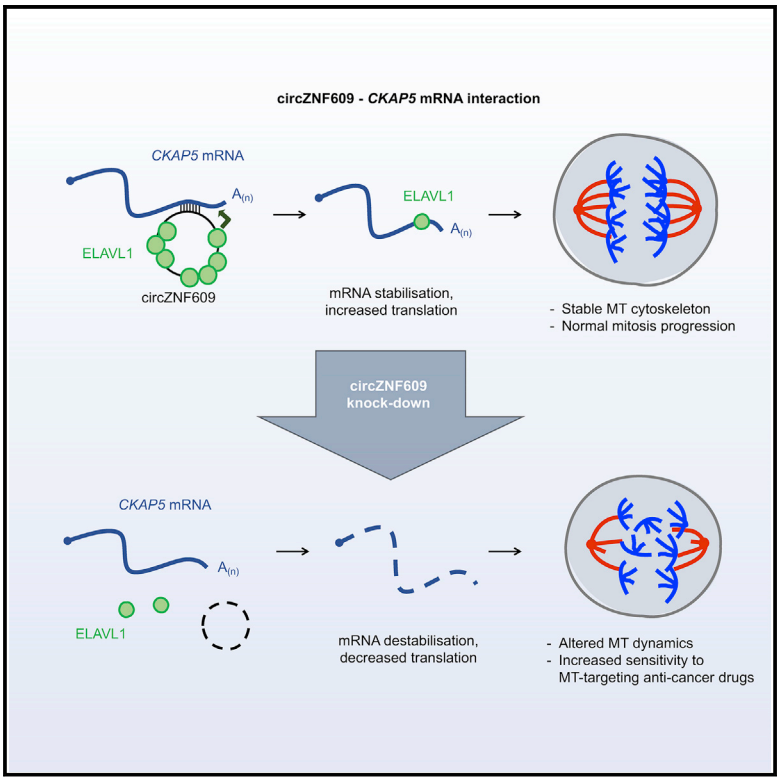

Highlights

- circZNF609 interacts with *CKAP5*, *UPF2*, and *SRRM1* mRNAs *in vivo*
- circZNF609-mRNA interaction increases ELAVL1 loading on the mRNAs
- ELAVL1 loading by circZNF609 regulates stability and translation of its targets
- CAKP5 regulation alters MT dynamics, sensitizing cells to chemotherapeutic drugs

Authors

Francesca Rossi, Manuel Beltran, Michela Damizia, ..., Maurizio Fanciulli, Patrizia Lavia, Irene Bozzoni

Correspondence

irene.bozzoni@uniroma1.it

In brief

In this article, Rossi et al. provide an interesting mechanism in which circZNF609-mRNA interaction increases translation, and among them, CKAP5 is a key factor in microtubule dynamics stability. The authors show how the disruption of RNA-RNA interactions is able to alter microtubule dynamics, sensitizing rhabdomyosarcoma cells to chemotherapeutic drugs.

Rossi et al., 2022, Molecular Cell *82*, 75–89
January 6, 2022 © 2021 The Author(s). Published by Elsevier Inc.
https://doi.org/10.1016/j.molcel.2021.11.032

CellPress

Molecular Cell

CellPress
OPEN ACCESS

Article

Circular RNA ZNF609/*CKAP5* mRNA interaction regulates microtubule dynamics and tumorigenicity

Francesca Rossi,[1,6] Manuel Beltran,[1,6] Michela Damizia,[1,2] Chiara Grelloni,[1] Alessio Colantoni,[3] Adriano Setti,[1] Gaia Di Timoteo,[1] Dario Dattilo,[1] Alvaro Centrón-Broco,[1] Carmine Nicoletti,[4] Maurizio Fanciulli,[5] Patrizia Lavia,[2] and Irene Bozzoni[1,3,7,*]

[1]Department of Biology and Biotechnology Charles Darwin, Sapienza University of Rome, Rome 00185, Italy
[2]Institute of Molecular Biology and Pathology CNR, Rome 00185, Italy
[3]Center for Life Nano- & Neuro-Science, Fondazione Istituto Italiano di Tecnologia (IIT), Rome 00161, Italy
[4]DAHFMO - Section of Histology and Medical Embryology, Sapienza University of Rome, Rome 00185, Italy
[5]UOSD SAFU, Department of Research, Diagnosis and Innovative Technologies, Translational Research Area, IRCCS Regina Elena National Cancer Institute, Rome 00144, Italy
[6]These authors contributed equally
[7]Lead contact
*Correspondence: irene.bozzoni@uniroma1.it
https://doi.org/10.1016/j.molcel.2021.11.032

SUMMARY

Circular RNAs (circRNAs) are widely expressed in eukaryotes and are regulated in many biological processes. Although several studies indicate their activity as microRNA (miRNA) and protein sponges, little is known about their ability to directly control mRNA homeostasis. We show that the widely expressed circZNF609 directly interacts with several mRNAs and increases their stability and/or translation by favoring the recruitment of the RNA-binding protein ELAVL1. Particularly, the interaction with *CKAP5* mRNA, which interestingly overlaps the back-splicing junction, enhances CKAP5 translation, regulating microtubule function in cancer cells and sustaining cell-cycle progression. Finally, we show that circZNF609 downregulation increases the sensitivity of several cancer cell lines to different microtubule-targeting chemotherapeutic drugs and that locked nucleic acid (LNA) protectors against the pairing region on circZNF609 phenocopy such effects. These data set an example of how the small effects tuned by circZNF609/*CKAP5* mRNA interaction might have a potent output in tumor growth and drug response.

INTRODUCTION

Many processes of gene expression control rely on RNA-based regulatory circuitries. To carry out these activities, RNA not only interacts with proteins but often directly pairs with other RNA molecules. In addition to the well-known activity of microRNAs (miRNAs) on mRNAs, much interest is now being directed to the study of how other non-coding RNAs control gene expression by targeting specific mRNAs to regulate their stability, translation, and localization (Fatica and Bozzoni, 2014; Statello et al., 2021). Along this line, growing interest is dedicated to circular RNAs (circRNAs), an emerging class of molecules originating from a back-splicing event in which a downstream splice-donor site is joined to an upstream splice-acceptor site, yielding a covalently closed circular RNA (Memczak et al., 2013; Salzman, 2016). The interest in studying circRNAs is raised because of several peculiar features, such as evolutionary conservation and tissue-specific expression, but above all, because their deregulated expression was linked to many pathological conditions, particularly cancer (Guarnerio et al., 2016; Patop and Kadener, 2018). Several studies indicate that circRNAs elicit their function as miRNA or protein sponges (Kristensen et al., 2019), but there is no evidence to date about their targeting activity on mRNAs. In this work, we studied circRNA zinc finger protein 609 (circZNF609), a circRNA previously described to be regulated and to control human primary myoblast and embryonal rhabdomyosarcoma (ERMS) cell proliferation (Legnini et al., 2017; Rossi et al., 2019; di Timoteo et al., 2020). CircZNF609 was found to also be upregulated in several types of human cancers, such as prostate cancer (Jin et al., 2019), breast cancer (Wang et al., 2018), gastric cancer (Wu et al., 2019; Liu et al., 2019), nasopharyngeal carcinoma (Zhu et al., 2019; Liu et al., 2021), and hepatocellular carcinoma (He et al., 2020), where its depletion has been linked with reduced aggressiveness of tumor cells. Although those studies pointed to circZNF609 as an miRNA sponge, we significantly advanced our understanding of the molecular mechanism through which it affects cell proliferation by focusing on its interactions with mRNAs. We found that circZNF609 pairs directly with a few mRNAs, among which is

This is an open access article under the CC BY-NC-ND license (http://creativecommons.org/licenses/by-nc-nd/4.0/).

CKAP5. As a result of such interaction, the *CKAP5* mRNA is stabilized and its translation is enhanced. We show that circZNF609 promotes the interaction between the *CKAP5* transcript and ELAVL1 (HuR), an RNA-binding protein (RBP) known to induce mRNA stabilization and translation (Galbán et al., 2008; Mazan-Mamczarz et al., 2003, 2008) and to control long noncoding RNA (lncRNA) metabolism (Legnini et al., 2014; Noh et al., 2016).

The CKAP5 protein is a highly conserved cytoskeleton-associated factor regulating several aspects of microtubule function: it promotes microtubule nucleation (Thawani et al., 2018), binds to their growing ("plus") ends, promotes their elongation, and regulates their dynamics (Brouhard et al., 2008). It also controls mitotic spindle formation and chromosome segregation by stabilizing kinetochore fibers, thus having an important role in mitotic progression (Cassimeris and Morabito, 2004; Miller et al., 2016).

Microtubule dynamics is essential to all processes depending on the cytoskeleton, including cell migration and differentiation, as well as the buildup of the mitotic apparatus and chromosome segregation. Several first-line chemotherapeutic agents, such as vincristine or paclitaxel/Taxol, are designed to target either the microtubule assembly from tubulin or their dynamic activity; they are effective chemotherapeutic agents and are still in use to treat cancer of various origin (Jordan and Wilson, 2004). Here, we demonstrate that preventing the circZNF609/*CKAP5* mRNA interaction, through either small interfering RNAs (siRNAs) against circZNF609 or locked nucleic acid (LNA)-modified oligonucleotides against the pairing region, sensitizes several cancer-model cell lines to microtubule-targeting chemotherapeutic agents, setting such blockage as a potential therapeutic strategy to improve cancer treatments.

RESULTS

CircZNF609 interacts with several mRNAs in rhabdomyosarcoma cells

To elucidate the molecular mechanism driving the cell cycle slow-down observed in myoblasts and ERMS cells upon circZNF609 knockdown (Legnini et al., 2017; Rossi et al., 2019), we started with the identification of the molecular partners of the circRNA. To detect specific RNA-RNA pairings occurring *in vivo*, we performed a pull-down of the endogenous circZNF609 using 4′-aminomethyl-4,5′,8-trimethylpsoralen (AMT) to crosslink rhabdomyosarcoma (RD) cells (an ERMS representative cell line). Two sets of biotinylated DNA probes (named Odd and Even, randomly) targeting *ZNF609* exon 2 were used (Figure 1A). All the circZNF609-targeting probes can pair to the exon 2, thereby recognizing both the circZNF609 and the linear *ZNF609* mRNA. We could not use a back-splicing junction (BSJ)-specific probe because its design for pull-down was suboptimal. As a negative control, we used a set of probes targeting a bacterial mRNA (*LacZ*).

After pull-down in two different biological replicates, enrichment for circZNF609 and *ZNF609* mRNA was tested. CircZNF609 was specifically enriched with both sets of probes, if compared with its linear counterpart or other non-specific RNAs, such as *GAPDH* mRNA (Figures 1B and S1A).

The replicate showing the best enrichment ratio between the circular versus linear *ZNF609* (Figure 1B) was subjected to high-throughput RNA sequencing. For target identification, reads were aligned to the reference genome, and peaks were considered positive when both Odd and Even coverages were at least 4-fold greater than both input and *LacZ* coverages. As shown in Figure 1C, we can detect reads only for *ZNF609* exon 2 but not for other parts of the linear transcript, indicating the preferential pull-down of circZNF609 RNA. We could identify several transcripts enriched in the pull-down (Table S1); to confirm their interaction, we performed a native RNA pull-down using either a mix of Odd and Even probes for the circRNA or probes for the control *LacZ* transcript. qRT-PCR allowed us to validate the interaction of many transcripts to circZNF609 (Figures 1D and S1B).

CircZNF609 binds ELAVL1 to regulate some of its mRNA interactors

We next focused on the putative proteins that might bind to the circRNA. The exon originating circZNF609 is reported to have eight binding sites for the ELAVL1 protein according to the CircInteractome database (Dudekula et al., 2016). ELAVL1 (HuR) is a member of the ELAV-like RBP family that generally binds to AU-rich elements in the 3′ UTR of mRNAs (Fan and Steitz, 1998), often stabilizing them (Brennan and Steitz, 2001) and enhancing their translation (Galbán et al., 2008; Mazan-Mamczarz et al., 2003, 2008). We performed data-mining analysis using published photoactivatable-ribonucleoside-enhanced cross-linking and immunoprecipitation (PAR-CLIP) sequencing data and confirmed that the second exon of *ZNF609* is bound by ELAVL1 at multiple sites in HEK293 cells (Kishore et al., 2011) (Figure 2A). To check whether ELAVL1 binds to circZNF609 in RD cells, we performed a UV-crosslinked RNA immunoprecipitation assay (CLIP) using an anti-ELAVL1 antibody, confirming this interaction *in vivo* (Figure 2B).

Interestingly, we observed a significant enrichment of ELAVL1 PAR-CLIP binding sites (Lebedeva et al., 2011) in mRNAs identified as interactors of circZNF609 (Figure 2C; Table S1). Of 29 mRNAs, 17 displayed ELAVL1 binding sites, implying that they could be potentially regulated by this protein. To validate the presence of ELAVL1 on these transcripts and to check whether this binding could be affected by circZNF609 depletion, we performed RNA immunoprecipitation (RIP) for ELAVL1 in control and circZNF609-downregulated RD cells. We confirmed the enrichment of circZNF609 in the RIP (Figure 2D); moreover, ELAVL1 immunoprecipitation pulled down some of the circZNF609 interactors, such as *CKAP5*, *UPF2*, and *SRRM1* mRNAs. Interestingly, the immunoprecipitation of these transcripts was reduced upon circZNF609 knockdown (Figures 2D and S2A), whereas it did not change for the negative control *GAPDH* mRNA and the positive control *CCNB1* mRNA, known to bind ELAVL1 (Wang et al., 2000) but not to interact with circZNF609 (Figure 2D). Other circZNF609-interacting mRNAs were not enriched in the RIP (Figure S2B), supporting the specificity of the interaction of ELAVL1 protein with *CKAP5*, *UPF2*, and *SRRM1* mRNAs and ruling out that their decreased enrichment upon circZNF609 depletion could be the consequence of the loss of circZNF609 co-purified RNA interactors. Importantly,

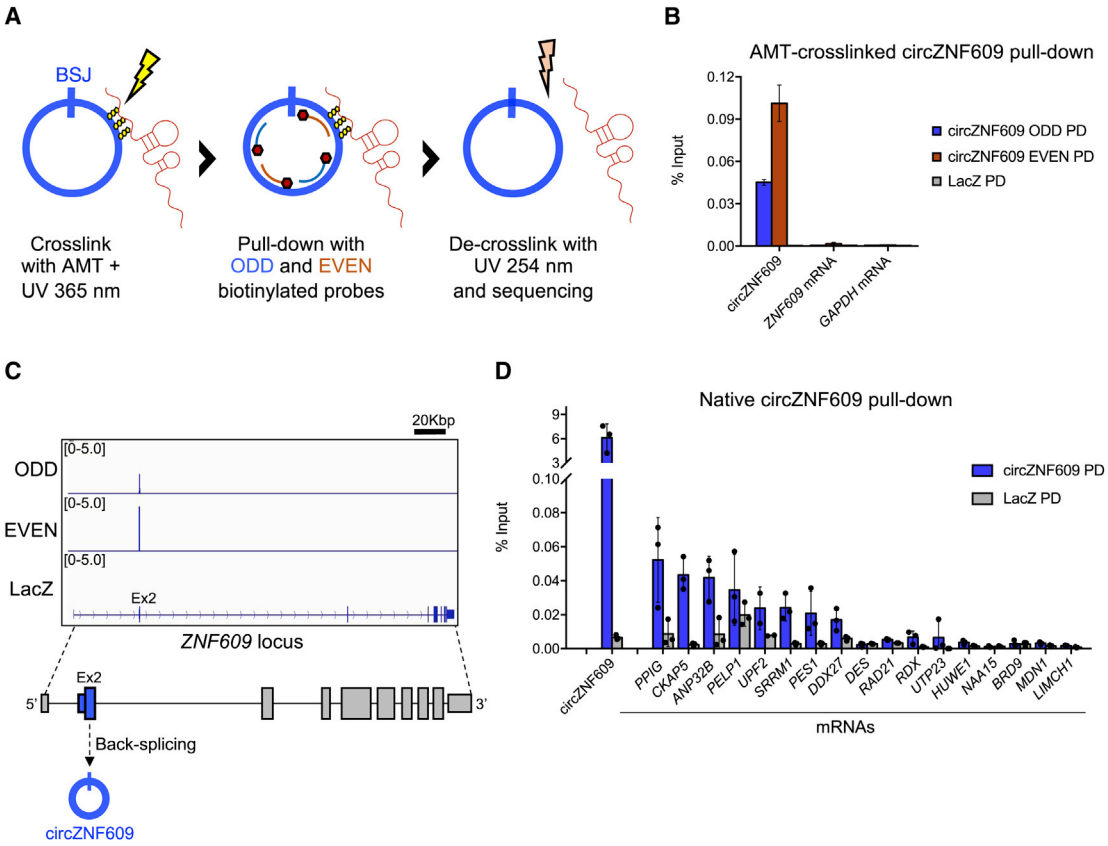

Figure 1. CircZNF609 interacts with several mRNAs in rhabdomyosarcoma cells

(A) Cartoon depicting the circZNF609 pull-down strategy. AMT, 4′-aminomethyl-4,5′,8-trimethylpsoralen; BSJ, back-splicing junction.

(B) qRT-PCR showing the enrichment of circZNF609, *ZNF609* mRNA, and *GAPDH* mRNA in the first replicate of the psoralen-crosslinked circZNF609 pull-down (PD) and control LacZ pull-down in RD cells. Data are shown as means of enrichment versus input ± SE of technical triplicates.

(C) Top: normalized RNA-sequencing read densities in *ZNF609* locus for Odd, Even, and LacZ pull-down. Bottom: cartoon depicting *ZNF609* locus and *ZNF609* exon 2 (Ex2)-derived circRNA (blue).

(D) qRT-PCR showing the enrichment of circZNF609 and its candidate mRNA interactors after native circZNF609 pull-down (PD) or control LacZ pull-down. n = 3. Data are shown as means of enrichment versus input ± SD.

See also Figure S1 and Table S1.

the ELAVL1 protein levels were not affected upon circRNA knockdown (Figure S2C). In conclusion these data indicate that the ELAVL1 binding to *CKAP5*, *UPF2*, and *SRRM1* mRNAs is dependent on circZNF609.

When the same RIP experiment was performed in the presence of LNA-modified oligonucleotides against the three major ELAVL1 CLIP signals on circZNF609 (Figure S2D), we observed a decreased interaction of ELAVL1 with *CKAP5*, *UPF2* and *SRRM1* mRNAs but not with control mRNAs, such as *GAPDH* and *CCNB1* (Figure 2E). Under these conditions, no change in the circZNF609 levels was observed (Figure S2E).

CircZNF609 regulates stability and translation of its target mRNAs via ELAVL1

Because circZNF609 is required for ELAVL1 binding to the *CKAP5*, *UPF2*, and *SRRM1* transcripts and considering the well-known activity of ELAVL1 on mRNA stability and translation, we analyzed RNA and protein levels of CKAP5, UPF2, and SRRM1 upon specific circZNF609 knockdown. Although circZNF609 downregulation had no effect on DDX27 (a negative control because it binds to circZNF609 but not to ELAVL1), a significant decrease (~50%) was observed in the CKAP5, UPF2, and SRRM1 proteins (Figure 3A). This outcome is specifically due to circZNF609 downregulation and not to its linear counterpart because siRNA against the linear *ZNF609* mRNA (si-Lin) had no significant effects on the CKAP5 protein levels (Figure S3A). To exclude off-target effects, we, instead, used a second siRNA targeting a region of circZNF609, which is in common with its linear *ZNF609* isoform (si-Circ+Lin), and we recapitulated the CKAP5 downregulation (Figure S3A).

Upon circZNF609 knockdown, we also observed a significant decrease of *CKAP5* mRNA (Figure 3A). Actinomycin D (ActD) treatment to inhibit transcription indicated that this was due to reduced mRNA stability (Figure 3B). We also checked the stability of *SRRM1* mRNA, whose levels upon circZNF609 depletion were variable, and we observed a significant decrease in its stability only after 2.5 h of ActD treatment (Figure 3B). Control transcripts (*DDX27*, *AURKA*, and *GAPDH*)

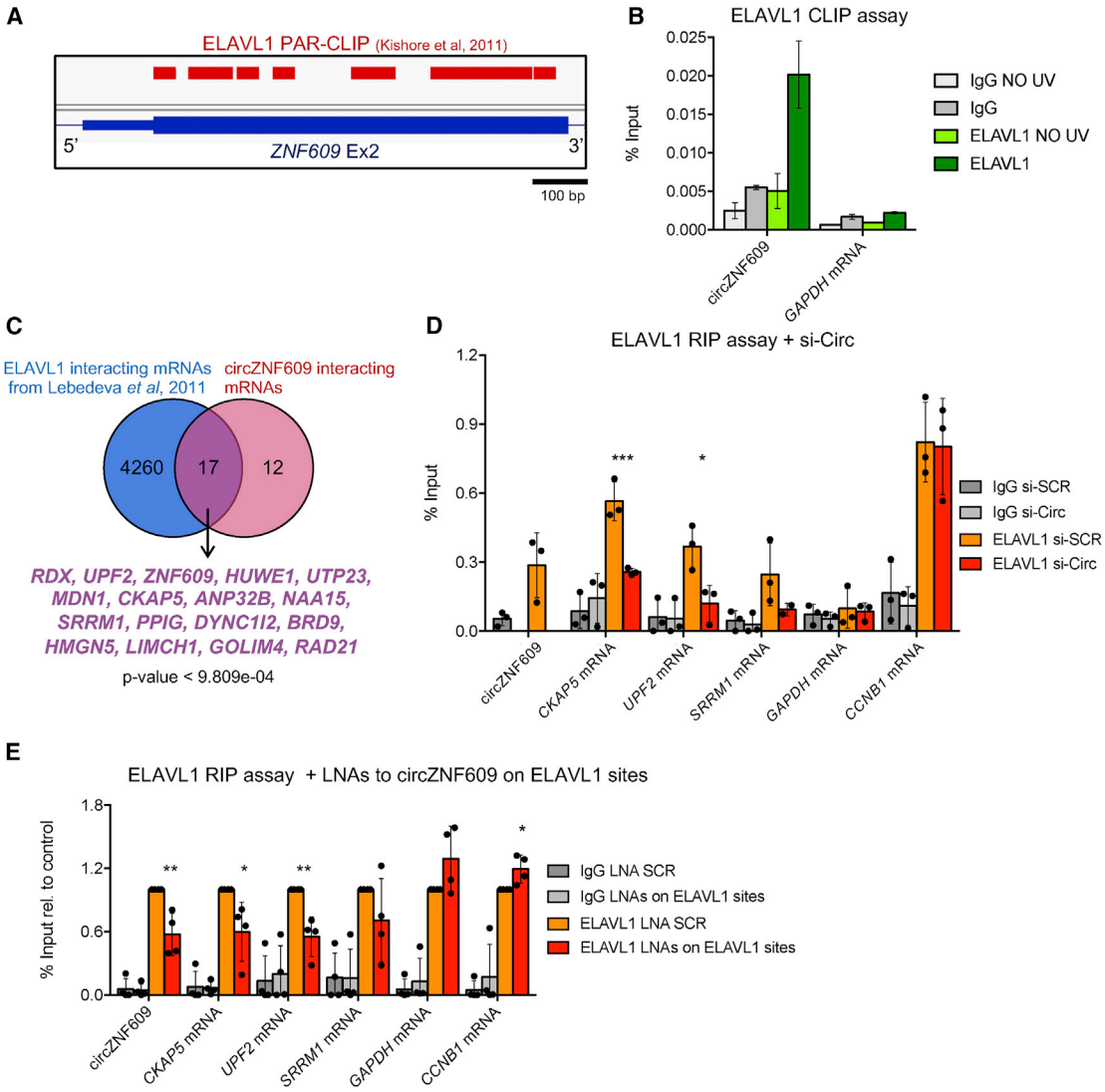

Figure 2. CircZNF609 interacts with ELAVL1 protein promoting ELAVL1 binding to some of its mRNA interactors

(A) Integrative Genomics Viewer (IGV) tracks for ELAVL1 PAR-CLIP crosslinked reads (red) from Kishore et al. (2011) on *ZNF609* exon 2.

(B) qRT-PCR showing circZNF609 and *GAPDH* mRNA enrichment in ELAVL1 CLIP assay in RD cells. n = 1. Data are shown as means of enrichment versus input ± SD.

(C) Venn diagram showing the intersection between ELAVL1 mRNA interactors from Lebedeva et al. (2011) and circZNF609 mRNA interactors.

(D) qRT-PCR showing the enrichment of several RNAs after ELAVL1 RIP in RD cells in control condition (si-SCR) or upon circZNF609 knockdown (si-Circ). n = 3. p referred to mRNA enrichment between si-Circ versus si-SCR = 0.0044 (*CKAP5* mRNA); and 0.0173 (*UPF2* mRNA). Data are shown as means of enrichment versus input ± SD. The ratio of each sample versus control was tested by two-tailed paired Student's t test.

(E) qRT-PCR showing the enrichment relative to control condition (ELAVL1 LNA SCR) of several RNAs after ELAVL1 RIP assay in RD cells upon transfection of LNAs targeting circZNF609 on ELAVL1 binding sites (LNAs on ELAVL1 sites). n = 4. p referred to RNA enrichment between LNAs on ELAVL1 sites versus LNA CTR = 0.006 (circZNF609); 0.029(*CKAP5* mRNA); 0.003(*UPF2* mRNA); and 0.027(*CCNB1* mRNA). Data are shown as means of enrichment versus input relative to control condition ± SD. The ratio of each sample versus control was tested by two-tailed unpaired Student's t test.

See also Figure S2.

showed no differential stability under either si-SCR or si-Circ conditions (Figure 3B).

To further investigate the specific effect on translation, we tested the ribosome association of *CKAP5*, *UPF2*, and *SRRM1* mRNAs in cells expressing a flagged ribosomal protein (60S ribosomal protein L22; RPL22) upon depletion of circZNF609 (Sousa Martins et al., 2016; Sanz et al., 2009). The results show that, indeed, the absence of the circRNA reduces the association of all three mRNAs to the ribosomes (Figures 3C, S3B, and S3C).

To correlate circZNF609 activity to its ability to recruit ELAVL1 onto its target mRNAs to promote their translation, we checked whether ELAVL1 knockdown, mediated by siRNAs, downregulates CKAP5 translation similar to circZNF609 depletion. A small, yet significant, effect on CKAP5 levels was observed

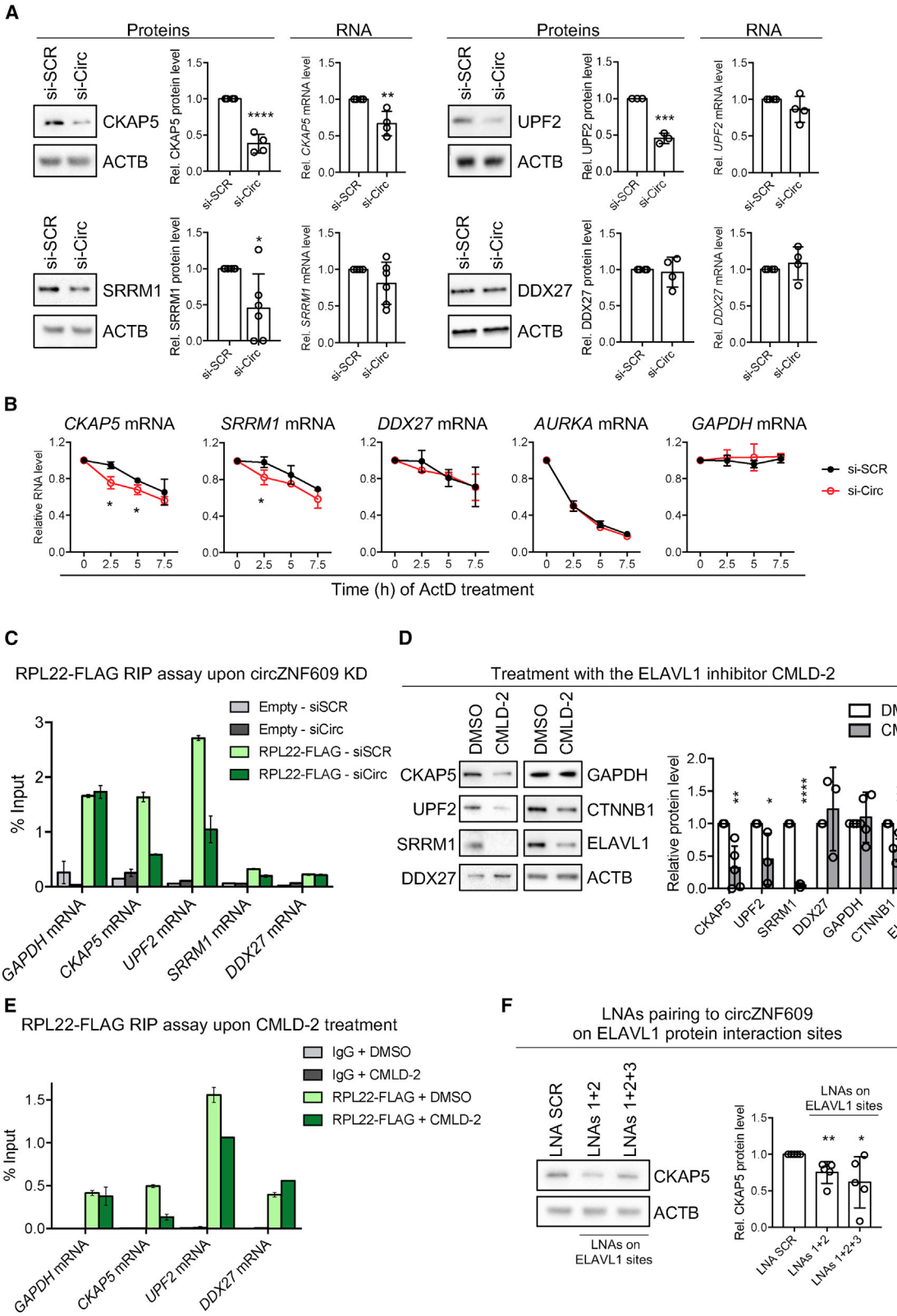

(legend on next page)

(Figure S3D); however, to circumvent the inefficient activity of the siRNAs on such an abundant protein, we treated cells with the specific ELAVL1-binding inhibitor CMLD-2 (Wu et al., 2015), and we measured the effects on CKAP5, UPF2, and SRRM1 protein levels (Figure 3D). With respect to positive CTNNB1 (Lebedeva et al., 2011; López de Silanes et al., 2003) and negative GAPDH and DDX27 controls, the translation of *CKAP5*, *UPF2*, and *SRRM1* mRNAs was significantly reduced (Figure 3D). Along the same line, their association to the ribosomes decreased upon inhibition of ELAVL1, as measured by RIP analysis in cells expressing the flagged RPL22 protein (Figures 3E, S3E, and S3F).

Finally, treatment with LNAs against the three major ELAVL1 binding sites on circZNF609 also produced a specific and significant decrease of CKAP5 levels (Figure 3F). Altogether, these data indicate the important role of ELAVL1 in the modulation of *CKAP5*, *UPF2*, and *SRRM1* mRNA translation.

The circZNF609 sequence across the BSJ interacts with *CKAP5* mRNA and regulates CKAP5 protein levels

As the CKAP5 protein has relevant roles in the cell cycle and mitotic progression and is also implicated in tumorigenesis, we decided to focus on its regulation as a model for this type of RNA-RNA interaction. *CKAP5* mRNA encodes for a highly conserved member of the XMAP215/ch-TOG family of microtubule (MT) polymerases regulating MT dynamics, chromosome segregation, and mitotic progression (Brouhard et al., 2008; Cassimeris and Morabito, 2004; Miller et al., 2016).

To map the RNA-RNA interactions between circZNF609 and *CKAP5* mRNA, as well as those of the other interactors, we used the IntaRNA program (Mann et al., 2017), also adapting its workflow for the analysis of the BSJ region. IntaRNA-predicted pairings are described in Figure S4A. The analysis predicted two putative interacting regions (Figures 4A and S4A): the first one involving the circZNF609 BSJ (nucleotides 802–866) and the nucleotides 6309–6417 of *CKAP5* mRNA (ENST00000529230), and the second one spanning the nucleotides 600–671 of circZNF609 and the nucleotides 6392–6470 of *CKAP5* mRNA (ENST00000529230). Both predictions involved a region in *CKAP5* 3′ UTR adjacent to three ELAVL1 binding sites belonging to the CU_nC type (i.e., $[CU_4]_3$) (Wein et al., 2003; Yeap et al., 2002) (Figure 4A, red highlights).

The analysis of published PAR-CLIP data confirmed that *CKAP5* 3′UTR is bound by ELAVL1 in HeLa (Lebedeva et al., 2011) and HEK293 (Kishore et al., 2011) cells and that the binding occurs exactly on the $[CU_4]_3$ motifs (Figure 4B).

To detect which one of the two regions predicted on circZNF609 was responsible for the interaction with the *CKAP5* mRNA, we performed native RNA pull-down experiments using antisense DNA oligonucleotides (Figure 4C) able to pair with either one of the two sequences and checked for co-enrichment of *CKAP5* mRNA. As shown in Figure 4D, the blocker oligonucleotides covering the BSJ region (BSJ blockers) did not reduce circZNF609 pull-down, although they significantly reduced *CKAP5* mRNA enrichment with respect to the control blocker (SCR blocker). As a control, the enrichment of *PPIG* mRNA, a transcript predicted to interact with circZNF609 in a different region, showed no significant changes (Figure S4B, left).

On the other hand, the Ex2 blocker oligonucleotide, covering the second circZNF609 sequence predicted to interact with *CKAP5* mRNA, produced no significant changes in *CKAP5* enrichment upon circZNF609 pull-down (Figure 4D). Specificity of the Ex2 blocker was proven by the reduced enrichment of the *PELP1* mRNA (Figure S4B, right), which is predicted to interact with circZNF609 at the level of the Ex2 blocker-targeted region (Figures 4C and S4A). These results indicate a crucial role for the circZNF609 BSJ region in mediating the interaction with the *CKAP5* mRNA.

To confirm these results *in vivo*, we transfected RD cells with LNA-modified oligonucleotides to block the same regions. Figure 4E (left) shows a significant decrease of CKAP5 protein levels when cells are treated with LNA-modified oligonucleotides covering the BSJ (LNAs BSJ) but not when either the control (LNA SCR) or the Ex2 region (LNA Ex2) LNAs were used. This effect was not accompanied by a downregulation of the circRNA (Figure 4E, right), underscoring that the downregulation of the CKAP5 protein levels is due to the blocking of the RNA-RNA

Figure 3. CircZNF609 sustains translation and stability of some of its mRNA interactors via ELAVL1

(A) Representative western blots and protein quantifications (relative to ACTB) and RNA levels (relative to *GAPDH* mRNA) of CKAP5 (from protein, $p < 0.0001$; from RNA, $p = 0.0073$), SRRM1 (from protein, $p = 0.0178$), UPF2 (from protein, $p = 0.0002$), and DDX27 in RD cells in control condition (si-SCR) or upon circZNF609 knockdown (si-Circ). $n \geq 3$. Data are shown as means of relative protein levels (or mean of fold changes) ± SD. The ratio of each sample versus control was tested by two-tailed unpaired Student's t test.

(B) qRT-PCRs showing mRNA stability upon actinomycin D (ActD) treatment in RD cells in control condition (si-SCR, black) or upon circZNF609 knockdown (si-Circ, red). $n = 3$. Referred to *CKAP5* mRNA stability, $p = 0.0116$ (2.5 h); 0.0385 (5 h). Referred to *SRRM1* mRNA stability, $p = 0.0482$ (2.5 h). Data are shown as means of fold changes ± SD. The ratio of each sample versus control was tested by two-tailed unpaired Student's t test.

(C) qRT-PCR showing the enrichment of circZNF609 interactors *CKAP5*, *UPF2*, *SRRM1*, and *DDX27* mRNAs, and control *GAPDH* mRNA in a representative RPL22-FLAG RIP assay in RD cells in control condition (si-SCR) or upon circZNF609 knockdown (si-Circ). Data are shown as means of enrichment versus input ± SD.

(D) Representative western blots and protein quantifications (relative to ACTB) of CKAP5 ($p = 0.0018$); UPF2 ($p = 0.0168$); SRRM1 ($p < 0.0001$); DDX27, GAPDH, and CTNNB1 ($p = 0.0008$); and ELAVL1 ($p < 0.0001$) in RD cells in control condition (DMSO) or upon treatment with CMLD-2. $n \geq 3$. Data are shown as means of relative protein levels ± SD. The ratio of each sample versus control was tested by two-tailed unpaired Student's t test.

(E) qRT-PCR showing the enrichment of circZNF609 interactors *CKAP5*, *UPF2*, and *DDX27* mRNAs, and control *GAPDH* mRNA in a representative RPL22-FLAG RIP assay in RD cells in control condition (DMSO) or upon treatment with CMLD-2. Data are shown as means of enrichment versus input ± SD.

(F) Representative western blot and protein quantification (relative to ACTB) of CKAP5 in RD cells in control condition (LNA SCR) or upon transfection of two different sets of LNAs targeting circZNF609 on ELAVL1 binding sites (LNAs 1+2, $p = 0.0060$; LNAs 1+2+3, $p = 0.0405$). $n = 5$. Data are shown as means of relative protein levels ± SD. The ratio of each sample versus control was tested by two-tailed unpaired Student's t test.

See also Figure S3.

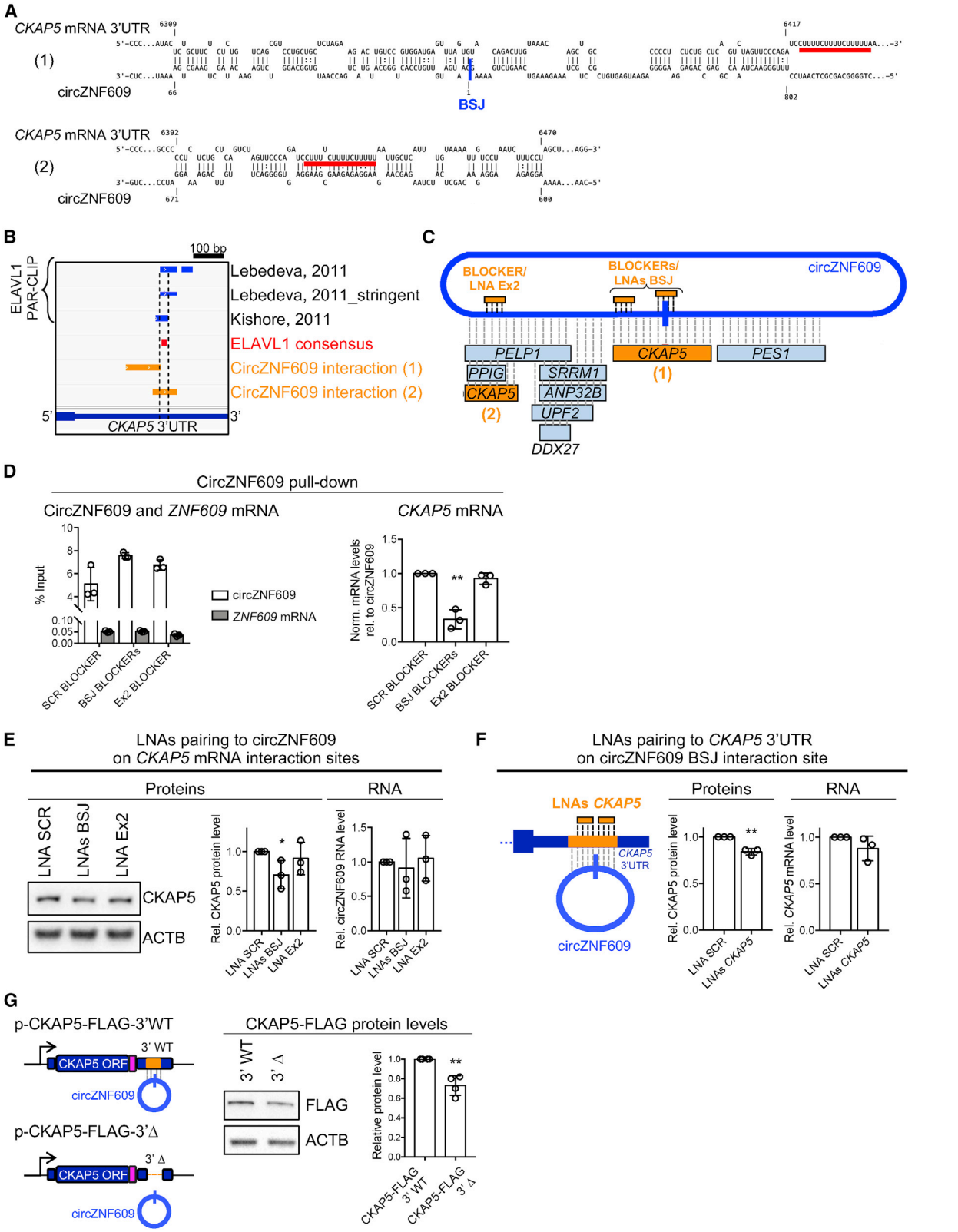

(legend on next page)

pairing. Because the BSJ is present in circZNF609, whereas it is absent in its linear counterpart, these data point to the specificity of the circRNA-mediated regulation on CKAP5.

This effect was further confirmed by a complementary experiment with LNAs against the region of the *CKAP5* mRNA, which pairs to circZNF609. Also in this case, we observed a slight but significant decrease of the CKAP5 protein levels (Figure 4F).

Because circZNF609 has been reported to work as a competing endogenous RNA for many miRNAs (He et al., 2020; Jin et al., 2019; Zhu et al., 2019; Liu et al., 2021; Wang et al., 2018; Wu et al., 2019; Liu et al., 2019), we checked whether the modulation of *CKAP5* mRNA by circZNF609 could be mediated by some miRNAs targeting both transcripts. We found no significant shared binding sites of microRNAs expressed in RD cells among circZNF609 and *CKAP5* mRNA (Figure S4C), ruling out an miRNA-mediated effect.

Finally, we made use of flagged CKAP5 constructs (Figure 4G, left) either wild-type (3′WT) or specifically deleted in the circZNF609 pairing region (3′Δ). The results demonstrate that the 3′Δ construct displays a significantly lower translation with respect to the WT (Figures 4G, right, and S4D). As a control, the 3′WT construct was shown to rely on the presence of circZNF609 for efficient translation (Figure S4E).

CircZNF609 knockdown destabilizes MT cytoskeleton, affecting mitotic progression and chromosome segregation

CKAP5 is a well-characterized MT polymerizing factor regulating the dynamic functions of the mitotic apparatus. Hence, we decided to explore whether circZNF609 can also regulate MT dynamics and mitotic events via CKAP5 protein-level modulation.

To study the overall effects of circZNF609 on MT dynamics, we analyzed the kinetics of cold-induced tubulin depolymerization after 20 min in ice (Figures 5A, left, and S5A). Mitotic cells were analyzed in control and circZNF609-depleted cultures. As shown in Figure 5A (right), although, in control cultures, most mitotic cells showed partially depolymerized spindles with MTs of remarkably lower density (pink bars), circZNF609 knockdown yielded accelerated MT depolymerization, revealed by the decrease in partially depolymerized spindles (91% in the control versus 81% in si-Circ; pink bars) and a concomitant 3-fold increase in cells with only residual fibers attached to kinetochores (K-fibers, 6% in control versus 19% in si-Circ; light blue bars). As expected, CKAP5-silenced cells (Figure S5B) showed an even more-extensive MT destabilization, with 61% of all mitoses displaying residual K-fibers (Figure 5A, right, light blue bars) and an increased frequency of mitoses with fully depolymerized spindles (dark blue bars).

We also measured the MT re-polymerization capacity in control or circZNF609-downregulated RD cells, by shifting the cultures to 37°C after prolonged incubation on ice (40 min) (Figure S5C). Figure S5D shows a time-course analysis of the progression of MT regrowth after the temperature shift. In circZNF609-downregulated cells, a significant reduction in MT repolymerization was observed at all examined time-points, compared with control mitoses (Figure S5E). Figure 5B (right) shows representative panels observed 4 min after temperature up-shift: although control cultures showed 29% of mitoses with reforming MT asters, in circZNF609 knockdown cultures (si-Circ), that phenotype still represented as many as 42% of mitoses (violet bars), whereas cells with partially and fully repolymerized MT phenotypes correspondingly decreased (pink and red bars). As expected, CKAP5 silencing exacerbated the depolymerization phenotype observed in circZNF609-depleted cells (Figure 5B, right) and strongly delayed MT regrowth at all time-points (Figure S5E).

Because circZNF609 affects the MT dynamics, we explored whether its knockdown induced mitotic abnormalities, exemplified in Figure 5C (left). We noticed a significant increase in

Figure 4. CircZNF609 back-splicing junction interacts with *CKAP5* mRNA and regulates CKAP5 protein levels

(A) Best IntaRNA interactions predicted between *CKAP5* mRNA and the BSJ-extended (top; 1) and not extended (bottom; 2) circZNF609 sequence. Red highlight indicates the ELAVL1 consensus binding sequence.

(B) IGV tracks for ELAVL1 PAR-CLIP crosslinked reads from Lebedeva et al. (2011) and Kishore et al. (2011) in the *CKAP5* 3′ UTR region. ELAVL1 consensus binding sequence is depicted in red; circZNF609 interacting regions is in orange.

(C) Cartoon depicting the IntaRNA predicted interactions between circZNF609 and its mRNA interactors. Colored rectangles represent interaction sites, with orange highlighting *CKAP5* mRNA interaction sites; the blue circle represents circZNF609 (vertical line: back-splicing junction); binding sites between circZNF609 and blockers/LNA oligonucleotides Ex2 and BSJ are depicted as thin orange rectangles.

(D) qRT-PCRs showing the enrichment of circZNF609, *ZNF609* mRNA, and *CKAP5* mRNA upon circZNF609 pull-down after the addition of either SCR, BSJ, or Ex2 oligo blockers in the lysate. n = 3. Data are shown as means of circZNF609 and *ZNF609* mRNA enrichment versus input ± SD (left) and means of *CKAP5* mRNA enrichment versus input relative to the control condition and corrected for the enrichment of circZNF609 ± SD (right). Referred to *CKAP5* mRNA enrichment in BSJ blockers condition, p = 0.0012. The ratio of each sample versus control was tested by two-tailed unpaired Student's t test.

(E) Representative western blot of CKAP5 and protein quantification (relative to ACTB) and circZNF609 RNA levels (relative to *GAPDH* mRNA) in RD cells after LNA SCR, LNAs BSJ, or LNA Ex2 transfection. n = 3. p = 0.0218. Data are shown as means of relative CKAP5 protein levels (or means of circZNF609 fold change) ± SD. The ratio of each sample versus control was tested by two-tailed unpaired Student's t test.

(F) Left: cartoon depicting the interaction between circZNF609 back-splicing junction and *CKAP5* mRNA 3′ UTR, with indication of the two LNAs *CKAP5* target sites on *CKAP5* mRNA 3′ UTR. Right: CKAP5 protein quantification (relative to ACTB; p = 0.0013) and *CKAP5* mRNA levels (rel. to *GAPDH* mRNA) in RD cells upon LNA SCR or LNAs *CKAP5* transfection. n = 3. Data are shown as means of relative CKAP5 protein levels (or means of *CKAP5* mRNA fold change) ± SD. The ratio of each sample versus control was tested by two-tailed unpaired Student's t test.

(G) Left: cartoon depicting the minigenes expressing *CKAP5-FLAG* mRNA with either its wild-type 3′ UTR (p-CKAP5-FLAG-3′WT) or a 3′ UTR deleted of the sequence interacting with circZNF609 back-splicing junction (p-CKAP5-FLAG-3′Δ). The FLAG tag is depicted in pink; the circZNF609-interacting region is in orange. The blue circle represents circZNF609. Right: representative western blot of CKAP5-FLAG and protein quantification (relative to ACTB) in RD cells after transfection (p = 0.0018). n = 4. Data are shown as means of relative protein levels ± SD. The ratio of each sample versus control was tested by two-tailed unpaired Student's t test.

See also Figure S4.

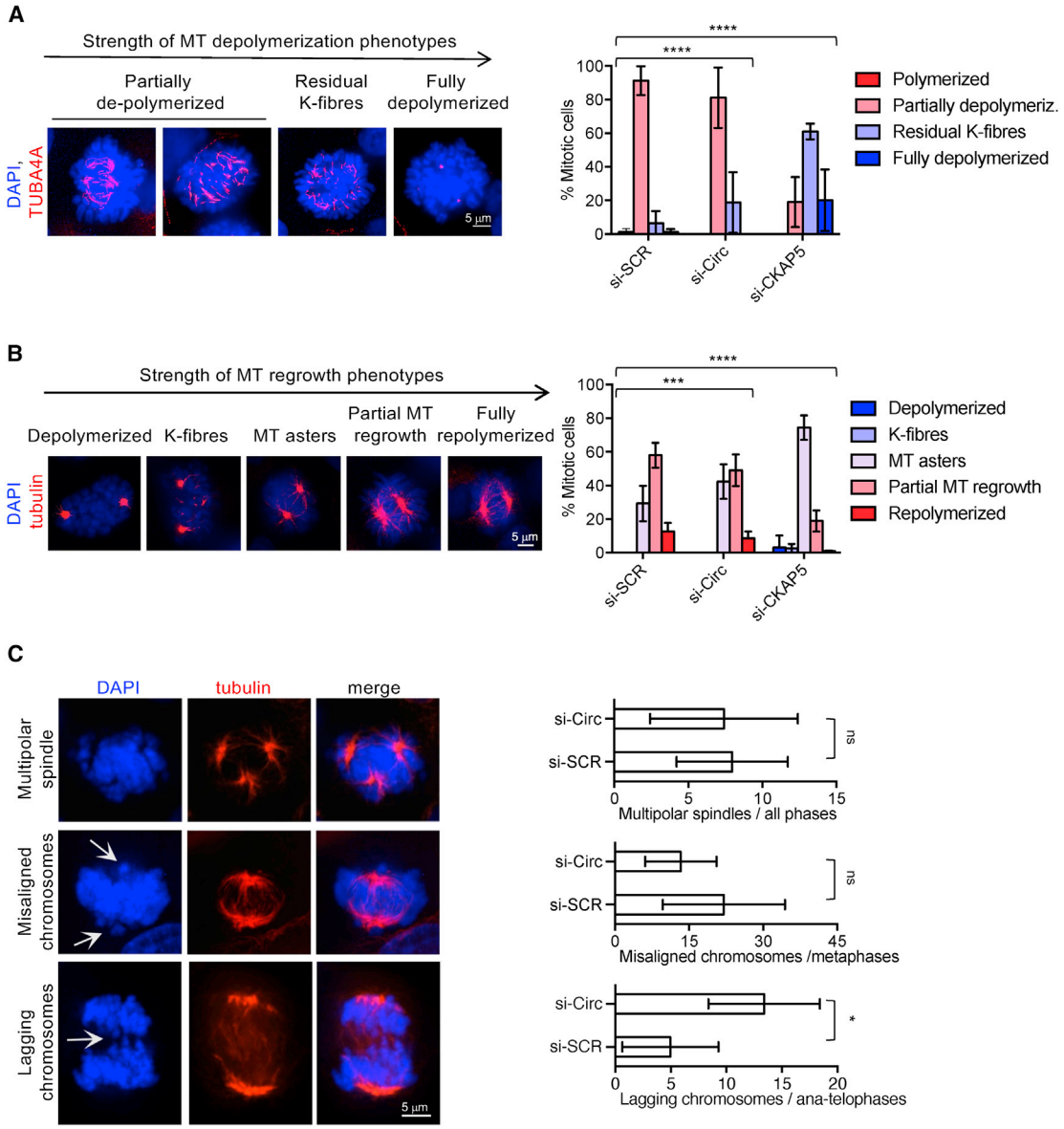

Figure 5. CircZNF609 knockdown destabilizes MT cytoskeleton, affecting mitotic progression and chromosome segregation

(A) Left: examples of MT (in red; TUBA4A staining) progressive depolymerization phenotypes observed in mitotic RD cells after incubation on ice (20 min). Chromosomes are stained with DAPI (blue). Bar, 5 μm. Right: histograms represent the frequency of MT phenotypes after cold incubation in control cultures (si-SCR) and in cultures silenced for either circZNF609 (si-Circ) or CKAP5 (si-CKAP5). n = 3. Differences in phenotype distributions were statistically analyzed using the multiple χ^2 test for trend (****$p < 0.0001$).

(B) Left: exemplifying panels of progressive MT regrowth. RD cells were stained as for (A) after incubation on ice (40 min) and rewarming to 37°C. Right: histograms representing the profile of MT regrowth phenotypes 4 min after temperature up-shift to 37°C. n = 4. Multiple χ^2 test for trend compare the phenotype distribution (***$p < 0.001$, ****$p < 0.0001$).

(C) Left: immunofluorescence (IF) panels exemplify frequently occurring mitotic abnormalities; RD cells were stained as for (B). Right: histograms representing the frequency of multipolar spindles (top), chromosome mis-alignment (middle; arrowed in left) and mis-segregating or lagging chromosomes (bottom; arrowed in left) in control (si-SCR) and circZNF609-downregulated (si-Circ) RD cells. n = 4. The χ^2 test compares each class in si-SCR versus si-Circ cultures (*$p < 0.05$). See also Figure S5.

lagging chromosomes in anaphase and telophase figures (5% in si-SCR versus 13% in si-Circ; Figure 5C, right), usually reflecting MT/chromosome misattachments that are not corrected by the spindle checkpoint and representing, therefore, a potential source of chromosome missegregation. Other mitotic abnormalities, such as multipolar spindles or metaphase chromosome misalignment, did not change significantly (Figure 5C, right).

Mitotic abnormalities, such as aneuploidy because of aberrant chromosome segregation, can lead to the accumulation of DNA

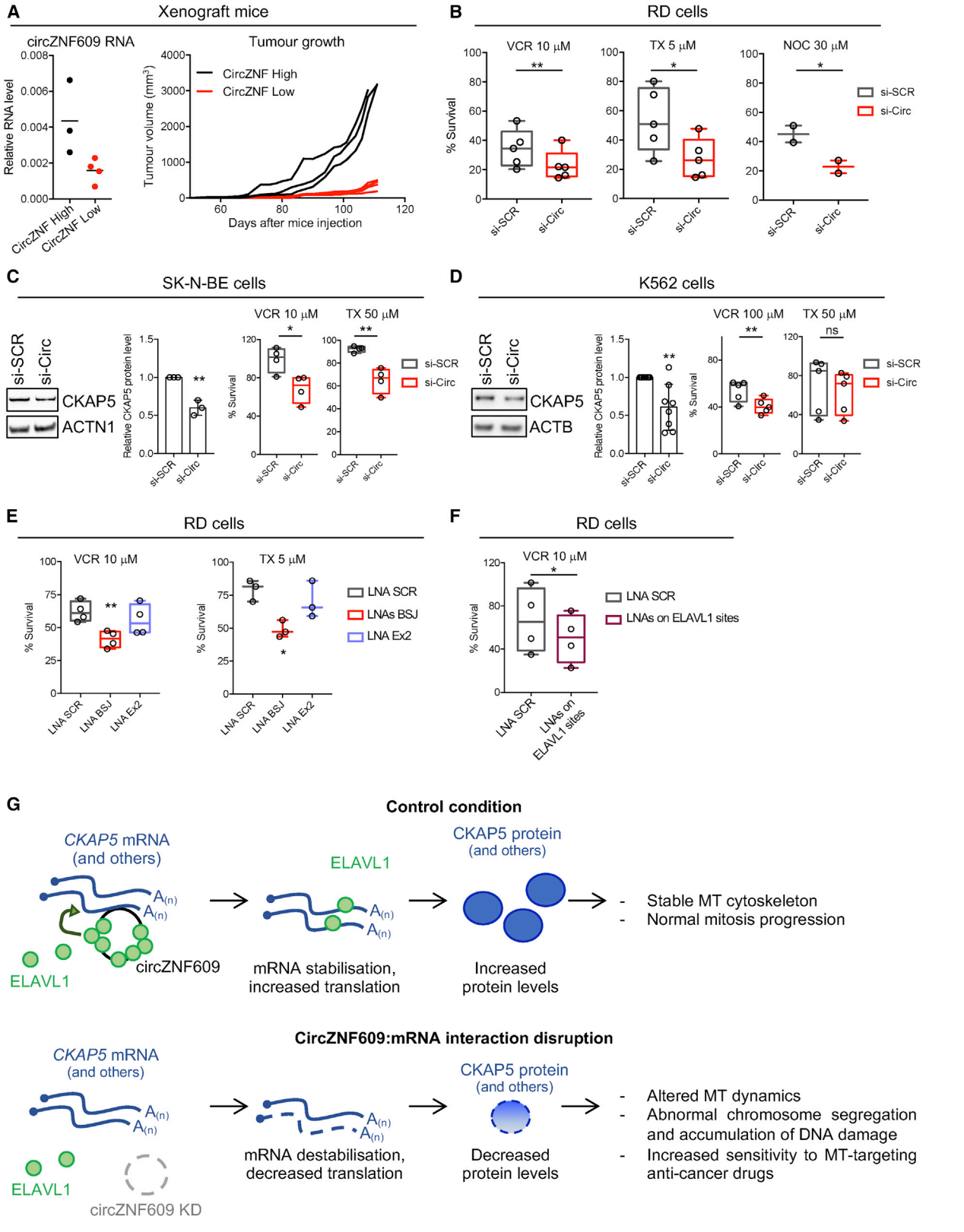

(legend on next page)

damage (Ganem and Pellman, 2012; Stingele et al., 2012; Williams et al., 2008).

Indeed, upon circZNF609 knockdown, we detected increased DNA damage measured by Comet assay (Figure S5F) and increased levels of a DNA-damage marker, phospho-H2AX histone (γ-H2AX) (Figures S5G and S5H).

Accumulation of damaged DNA from CKAP5-dependent mitotic alterations could be responsible for the slow-down of the following G1-S transition previously observed upon circZNF609 depletion (Rossi et al., 2019). Indeed, we found G1-S transition and chromosome segregation markers to be downregulated, with only an exception for cyclins, upon CKAP5 depletion as much as upon circZNF609 knockdown (Figure S5I).

CircZNF609 knockdown can strengthen the anti-tumor effects of MT-targeting drugs

The reduced ERMS cell proliferation rate obtained upon circZNF609 knockdown might be associated with decreased *in vivo* tumorigenic capability. To test that hypothesis, we performed mouse xenograft growth assays of RD cells expressing a short hairpin RNA (shRNA) against circZNF609 under doxycycline induction. We grouped the mice according to circZNF609 expression levels in their tumors (Figure 6A, left), and we observed that those containing low levels of circZNF609 developed smaller tumors (Figure 6A, right), thus reinforcing the previously observed data linking circZNF609 to tumor growth.

The link between MT function and cancer was established more than a century ago (Boveri, 1902; Gönczy, 2015), and, indeed, MTs are still among the best-validated chemotherapeutic targets in cancer treatment (Jordan and Wilson, 2004). One of the standard chemotherapeutic treatments for intermediate-/high-risk rhabdomyosarcoma (RMS) involves a drug cocktail that includes vincristine (Panda et al., 2017), which impairs MT polymerization by sequestering tubulin monomers, hence blocking mitosis (Jordan, 2012). Other MT-targeting drugs include nocodazole (Vasquez et al., 1997) and paclitaxel/Taxol (Horwitz, 1992; Vasquez et al., 1997).

Because of circZNF609-knockdown-induced MT instability, we checked whether this phenotype could be translated into an enhanced sensitivity to different MT-targeting chemotherapeutics. As shown in Figure 6B, siRNA-mediated circZNF609 downregulation in RD cells resulted in a decreased survival rate compared with the control condition, upon treatment with either 10 μM vincristine, 5 μM Taxol, or 30 μM nocodazole.

To underscore the broad importance of the fine tuning of MT regulation by circZNF609, we tried to export the above findings in other cancer cell lines. Figure 6C shows that the specific knockdown of circZNF609 (Figure S6A) in the SK-N-BE neuroblastoma cells also produced a downregulation of the CKAP5 protein (Figure 6C, left) and increased their sensitivity to a 24-h treatment with vincristine and Taxol (Figure 6C, right). Similar experiments performed in the K562 chronic myelogenous leukemia cell line confirmed this regulation is a widespread phenomenon (Figures 6D and S6B).

Finally, we tested whether these effects could be reproduced when blocking circZNF609-*CKAP5* mRNA interaction through LNA-treatment. As shown in Figure 6E, RD cells treated with the LNAs against circZNF609 BSJ (LNA BSJ) were significantly more sensitive to vincristine and Taxol with respect to cells transfected with control LNA (LNA SCR). On the other hand, cells treated with the LNA Ex2 showed no altered sensitivity to these drugs (Figure 6E). In addition, cells treated with LNAs covering the three major ELAVL1 sites on circZNF609 were significantly more sensitive to vincristine treatment (Figure 6F), underscoring the importance of ELAVL1 in this phenomenon.

DISCUSSION

Although some subtypes of RNA-RNA pairings, such as those involving the miRNA/mRNA regulatory networks, are widely studied, little is known about other kinds of interactions occurring among RNAs with larger sizes. Specific interest concerns the ability of non-coding RNAs to trigger the formation of functional ribonucleoprotein (RNP) complexes by acting as scaffolds for proteins and RNA assemblies. In this study, we identified a

Figure 6. Loss of circZNF609/*CKAP5* mRNA interaction strengthens the anti-tumor effects of MT-targeting drugs

(A) Left: qRT-PCR representing circZNF609 RNA levels in xenograft mice (n = 3 in circZNF-high group, black; n = 4 in circZNF-low group, red); data are shown as individual dots representing $\Delta\Delta C_t$ values relative to *GAPDH* mRNA; horizontal bars represent the mean. Right: graph showing tumor volume (mm^3) over time (days after mice injection) in circZNF-high (black) and in circZNF-low (red) mice.

(B) Boxplots representing the percentage of survival of RD cells either in control condition (si-SCR, gray) or in circZNF609 knockdown (si-Circ, red), upon treatment with either vincristine (VCR; n = 5; p = 0.0051), Taxol (TX; n = 5; p = 0.0189), or nocodazole (NOC; n = 2; p = 0.0394). The ratio of each sample versus control was tested by two-tailed paired (VCR and TX) or unpaired (NOC) Student's t test.

(C) Left: representative western blot showing CKAP5 protein levels in SK-N-BE cells in si-SCR and si-Circ, and protein quantifications relative to ACTN1 (n = 3; p = 0.0023). Right: as in (B), in SK-N-BE cells; VCR: n = 4, p = 0.0200; TX: n = 4, p = 0.0030. The ratio of each sample versus control was tested by two-tailed unpaired Student's t test.

(D) As in (C), in K562 cells. Left: ACTB hybridization used as loading control; n = 8; p = 0.0025. Right: VCR: n = 5, p = 0.0078; TX: n = 5. The ratio of each sample versus control was tested by two-tailed unpaired (protein analysis) or paired (cell survival analysis) Student's t test.

(E) Boxplots representing the percentage of survival of RD cells transfected with either the control LNA SCR (gray), the LNAs BSJ (red), or the LNA Ex2 (violet) upon treatment with either VCR (n = 4; p LNAs BSJ versus LNA SCR = 0.0057) or TX (n = 3; p LNAs BSJ versus LNA SCR = 0.0262). The ratio of each sample versus control was tested by two-tailed unpaired Student's t test.

(F) Boxplots representing the percentage of survival of RD cells upon transfection of either control LNA SCR (black) or LNAs targeting circZNF609 on ELAVL1 sites (LNAs on ELAVL1 sites, purple) upon treatment with VCR (n = 4; p = 0.0326). The ratio of the sample versus control was tested by two-tailed paired Student's t test.

(G) Cartoon depicting the molecular circuit involving circZNF609, *CKAP5*, and other mRNAs and the ELAVL1 protein.

See also Figure S6.

novel type of functional interaction between a circRNA and specific mRNAs. We demonstrate that circZNF609 can specifically pair *in vivo* with several mRNAs. Notably, these mRNAs were not in the top-tier list derived by IntaRNA predictions and other similar programs that calculate RNA-RNA interaction based on the free energy of complementarity and accessibility, indicating that this parameter is not the unique feature required for the functional interaction. On some of our validated targets (*CKAP5*, *UPF2*, and *SRRM1* mRNAs), relatively long regions (around 80–130 nucleotides) containing stretches of discontinuous pairing were found, whereas other *in silico*-derived targets with similar predicted interactions could not be validated. Therefore, other features, such as structure, localization, binding proteins, might be determinants to establish productive RNA-RNA interactions.

We discovered that the circZNF609 interaction with *CKAP5, UPF2*, and *SRRM1* mRNAs controlled their stability and translation through the recruitment of the ELAVL1 RNA-binding protein. ELAVL1 is an abundant RNA-interacting protein and many cellular targets are known which might compete for its binding. CircZNF609, which has seven ELAVL1 binding sites, can act as a carrier for the download of this protein on interacting mRNAs thanks to the proximity given by their physical interaction. In the case of *CKAP5* mRNA, which has only one specific ELAVL1 binding site in the 3′ UTR (Lebdeva et al., 2011), this cooperation would be necessary to compete with the other ELAVL1 cellular targets. The absolute stoichiometry between circZNF609 and the other RNAs would be less critical because this process is expected to be a dynamic one in which circZNF609 can undergo subsequent cycles of ELAVL1 upload and download.

For the other circZNF609-interacting mRNAs which also bind ELAVL1, we did not further investigate the functional consequences of these interactions. Because ELAVL1 has been shown to regulate RNA metabolism at many different levels, both in the nucleus (Legnini et al., 2014) and in the cytoplasm (Noh et al., 2018), it is possible that each individual transcript uses ELAVL1 for different regulatory means. Moreover, it has been shown that ELAVL1 can control cell proliferation, apoptosis, senescence, and other cellular pathways, contributing to many diseases, such as cancer (Srikantan and Gorospe, 2012). A more-detailed analysis along this direction will enable the elucidation of the pleiotropy of such control, allowing us to establish the functional role of the different circZNF609-mRNAs-ELAVL1 RNPs.

The effect of circZNF609 on the control of CKAP5 protein levels and, in turn, on the dynamic functions of the mitotic apparatus and on proliferation (Figure 6G) is quite relevant when considering the upregulation of this RNA in several different tumors (He et al., 2020; Jin et al., 2019; Zhu et al., 2019; Liu et al., 2021; Wang et al., 2018; Wu et al., 2019; Liu et al., 2019). Because we show that the circZNF609/CKAP5 axis described in RD also operates in other cancer cell lines, we believe that we have underscored a mechanism that can justify the role of this RNA in many different tumorigenic conditions. So far, circRNAs have been implicated in cancer mainly through their miRNA sponging activity (Kristensen et al., 2019); however, this feature restricts their function mostly because of the exclusive microRNA signature that specifies each type of tumor. In the case of circZNF609, sponging activity has been suggested against different miRNAs in different tumors (He et al., 2020; Jin et al., 2019; Zhu et al., 2019; Liu et al., 2021; Wang et al., 2018; Wu et al., 2019; Liu et al., 2019). Instead, the regulation here described, involving the ubiquitous CKAP5 protein, would operate in all tumor cells in which circZNF609 is overexpressed, regardless of the cancer histological origin or its miRNA signature. Finally, because the *CKAP5* mRNA-circZNF609 interaction occurs at the level of the BSJ, which is unique to the circular RNA, it is possible to exclude any contribution of the linear *ZNF609* mRNA counterpart to the observed phenotype.

Another important outcome of our work is that we observed the synergistic effect when circZNF609 downregulation was combined with different MT-targeting drugs. These results open the intriguing perspective of using circZNF609 as a novel therapeutic target because of its ability to modulate the response of cancer cells to widely used chemotherapeutics. Because its mode of action is through direct pairing to *CKAP5* mRNA, our data demonstrate that the use of either siRNAs against circZNF609 or LNA-modified oligonucleotides preventing RNA-RNA interaction could represent possible adjunctive therapeutic strategies to prevent tumor growth. Moreover, because the region of pairing includes the BSJ, this approach would ensure the specificity of the treatment for the circular form without any possible effect on the linear *ZNF609* mRNA counterpart. With the actual emphasis on RNA therapeutics demonstrated by the increasing number of oligonucleotide drugs already in clinical trials (Wang et al., 2020), we believe that RNA-RNA interactions could be a mother lode in which to find interesting targets for new RNA-based treatments.

Limitations of the study

We have not investigated the degree of evolutionary conservation of this process in other mammalian systems, and we have restricted the analysis to the effect of ELAVL1 on the CKAP5 factor because of its important role in the control of cell proliferation. In addition to ELAVL1, additional factors could concur with the described regulatory process both for CKAP5 and the other targets.

STAR★METHODS

Detailed methods are provided in the online version of this paper and include the following:

- KEY RESOURCES TABLE
- RESOURCE AVAILABILITY
  - Lead contact
  - Materials availability
  - Data and code availability
- EXPERIMENTAL MODEL AND SUBJECT DETAILS
  - Cell cultures
  - Xenograft mice establishment and tumor measurements
- METHOD DETAILS
  - Plasmid construction
  - Cell transfection

- Establishment of an RD cell line expressing a circZNF609-targeting shRNA
- Actinomycin D cell treatment for RNA analysis
- CMLD-2 cell treatment for protein analysis
- Microtubule-targeting drug cell treatments
- Western blot
- RNA isolation and analysis
- RNA pull-down
- RNA Immunoprecipitation assays
- COMET assay
- Immunofluorescence
- Microtubule de-polymerization and re-polymerization assays and analysis of mitotic phenotypes
- RNA-Sequencing bioinformatic analyses
- Prediction of RNA-RNA interacting regions
- miRNA analysis

● QUANTIFICATION AND STATISTICAL ANALYSIS

SUPPLEMENTAL INFORMATION

Supplemental information can be found online at https://doi.org/10.1016/j.molcel.2021.11.032.

ACKNOWLEDGMENTS

We thank Prof. A. Fatica's laboratory and Prof. E. Ferretti's laboratory for providing cell lines; Prof. A. Rosa's laboratory and Prof. G. Meister's laboratory for providing plasmids; M. Guarnacci, Dr. D. Mariani, Prof. A. Musarò, Prof. F. Megiorni, and Dr. S. Camero for useful discussions; M. Marchioni and M. Arceci for technical help; and B. Amadio for assistance in animal experiments. This work was supported by grants from AIRC (IG 2019 no. 23053); ERC-2019-SyG (855923 ASTRA); European Union's Horizon 2020 research and innovation programme under the Marie Sklodowska-Curie grant agreement no. 721890; PRIN 2017 (2017P352Z4 and 2017FNZRN3); and H2020 Program "Sapienza Progetti Collaborativi."

AUTHOR CONTRIBUTIONS

F.R. and M.B. co-designed and performed most of the experiments. M.D. and P.L. performed microtubule-related experiments. A.C. and A.S. performed bioinformatical analyses. C.G., G.D.T., D.D., and A.C.-B. helped in the experimental part. M.F. and C.N. coordinated and performed xenograft mice experiments. F.R., M.B., P.L., and I.B. wrote the manuscript with inputs from all the authors. I.B. co-designed, supervised, and coordinated the work.

DECLARATION OF INTERESTS

The authors declare no competing interests.

Received: June 3, 2021
Revised: October 7, 2021
Accepted: November 23, 2021
Published: December 22, 2021

REFERENCES

Barnett, D.W., Garrison, E.K., Quinlan, A.R., Strömberg, M.P., and Marth, G.T. (2011). BamTools: A C++ API and toolkit for analyzing and managing BAM files. Bioinformatics *27*, 1691–1692.

Beltran, M., Tavares, M., Justin, N., Khandelwal, G., Ambrose, J., Foster, B.M., Worlock, K.B., Tvardovskiy, A., Kunzelmann, S., Herrero, J., et al. (2019). G-tract RNA removes Polycomb repressive complex 2 from genes. Nat. Struct. Mol. Biol. *26*, 899–909.

Bersani, F., Lingua, M.F., Morena, D., Foglizzo, V., Miretti, S., Lanzetti, L., Carrà, G., Morotti, A., Ala, U., Provero, P., et al. (2016). Deep sequencing reveals a novel miR-22 regulatory network with therapeutic potential in rhabdomyosarcoma. Cancer Res. *76*, 6095–6106.

Bolger, A.M., Lohse, M., and Usadel, B. (2014). Trimmomatic: A flexible trimmer for Illumina sequence data. Bioinformatics *30*, 2114–2120.

Boveri, T. (1902). Über mehrpolige mitosen als mittel zur analyse des zellkerns. Verhandl. Phys.-Med. Ges. Würzburg *35*, 67–90.

Brennan, C.M., and Steitz, J.A. (2001). HuR and mRNA stability. Cell. Mol. Life Sci. *58*, 266–277.

Brouhard, G.J., Stear, J.H., Noetzel, T.L., Al-Bassam, J., Kinoshita, K., Harrison, S.C., Howard, J., and Hyman, A.A. (2008). XMAP215 is a processive microtubule polymerase. Cell *132*, 79–88.

Cassimeris, L., and Morabito, J. (2004). TOGp, the human homolog of XMAP215/Dis1, is required for centrosome integrity, spindle pole organization, and bipolar spindle assembly. molecular biology of the cell. Mol. Biol. Cell *15*, 1580–1590.

di Timoteo, G., Dattilo, D., Centrón-Broco, A., Colantoni, A., Guarnacci, M., Rossi, F., Incarnato, D., Oliviero, S., Fatica, A., Morlando, M., et al. (2020). Modulation of circRNA metabolism by m6A modification. Cell Rep. *31*, 107641.

Dobin, A., Davis, C.A., Schlesinger, F., Drenkow, J., Zaleski, C., Jha, S., Batut, P., Chaisson, M., and Gingeras, T.R. (2013). STAR: ultrafast universal RNA-seq aligner. Bioinformatics *29*, 15–21.

Dudekula, D.B., Panda, A.C., Grammatikakis, I., De, S., Abdelmohsen, K., and Gorospe, M. (2016). CircInteractome: A web tool for exploring circular RNAs and their interacting proteins and microRNAs. RNA Biol. *13*, 34–42.

Fan, X.C., and Steitz, J.A. (1998). Overexpression of HuR, a nuclear-cytoplasmic shuttling protein, increases the in vivo stability of ARE-containing mRNAs. EMBO J. *17*, 3448–3460.

Fatica, A., and Bozzoni, I. (2014). Long non-coding RNAs: New players in cell differentiation and development. Nat. Rev. Genet. *15*, 7–21.

Galbán, S., Kuwano, Y., Pullmann, R., Jr., Martindale, J.L., Kim, H.H., Lal, A., Abdelmohsen, K., Yang, X., Dang, Y., Liu, J.O., et al. (2008). RNA-binding proteins HuR and PTB promote the translation of hypoxia-inducible factor 1α. Mol. Cell. Biol. *28*, 93–107.

Ganem, N.J., and Pellman, D. (2012). Linking abnormal mitosis to the acquisition of DNA damage. J. Cell Biol. *199*, 871–881.

Gönczy, P. (2015). Centrosomes and cancer: Revisiting a long-standing relationship. Nat. Rev. Cancer *15*, 639–652.

Guarnerio, J., Bezzi, M., Jeong, J.C., Paffenholz, S.V., Berry, K., Naldini, M.M., Lo-Coco, F., Tay, Y., Beck, A.H., and Pandolfi, P.P. (2016). Oncogenic role of fusion-circRNAs derived from cancer-associated chromosomal translocations. Cell *165*, 289–302.

He, Y., Huang, H., Jin, L., Zhang, F., Zeng, M., Wei, L., Tang, S., Chen, D., and Wang, W. (2020). CircZNF609 enhances hepatocellular carcinoma cell proliferation, metastasis, and stemness by activating the Hedgehog pathway through the regulation of miR-15a-5p/15b-5p and GLI2 expressions. Cell Death Dis. *11*, 358.

Horwitz, S.B. (1992). Mechanism of action of taxol. Trends Pharmacol. Sci. *13*, 134–136.

Jin, C., Zhao, W., Zhang, Z., and Liu, W. (2019). Silencing circular RNA circZNF609 restrains growth, migration and invasion by up-regulating microRNA-186-5p in prostate cancer. Artif. Cells Nanomed. Biotechnol. *47*, 3350–3358.

Jordan, M. (2012). Mechanism of action of antitumor drugs that interact with microtubules and tubulin. Curr. Med. Chem. Anticancer Agents *2*, 1–17.

Jordan, M.A., and Wilson, L. (2004). Microtubules as a target for anticancer drugs. Nat. Rev. Cancer *4*, 253–265.

Keene, J.D., Komisarow, J.M., and Friedersdorf, M.B. (2006). RIP-Chip: The isolation and identification of mRNAs, microRNAs and protein components of ribonucleoprotein complexes from cell extracts. Nat. Protoc. *1*, 302–307.

Kishore, S., Jaskiewicz, L., Burger, L., Hausser, J., Khorshid, M., and Zavolan, M. (2011). A quantitative analysis of CLIP methods for identifying binding sites of RNA-binding proteins. Nat. Methods *8*, 559–564.

Kristensen, L.S., Andersen, M.S., Stagsted, L.V.W., Ebbesen, K.K., Hansen, T.B., and Kjems, J. (2019). The biogenesis, biology and characterization of circular RNAs. Nat. Rev. Genet. *20*, 675–691.

Lebedeva, S., Jens, M., Theil, K., Schwanhäusser, B., Selbach, M., Landthaler, M., and Rajewsky, N. (2011). Transcriptome-wide analysis of regulatory interactions of the RNA-binding protein HuR. Mol. Cell *43*, 340–352.

Legnini, I., Morlando, M., Mangiavacchi, A., Fatica, A., and Bozzoni, I. (2014). A feedforward regulatory loop between HuR and the long noncoding RNA linc-MD1 controls early phases of myogenesis. Mol. Cell *53*, 506–514.

Legnini, I., Di Timoteo, G., Rossi, F., Morlando, M., Briganti, F., Sthandier, O., Fatica, A., Santini, T., Andronache, A., Wade, M., et al. (2017). Circ-ZNF609 is a circular rna that can be translated and functions in myogenesis. Mol. Cell *66*, 22–37.e9.

Li, H., Handsaker, B., Wysoker, A., Fennell, T., Ruan, J., Homer, N., Marth, G., Abecasis, G., and Durbin, R.; 1000 Genome Project Data Processing Subgroup (2009). The Sequence Alignment/Map format and SAMtools. Bioinformatics *25*, 2078–2079.

Li, J.-H., Liu, S., Zhou, H., Qu, L.-H., and Yang, J.-H. (2014). starBase v2.0: Decoding miRNA-ceRNA, miRNA-ncRNA and protein-RNA interaction networks from large-scale CLIP-Seq data. Nucleic Acids Res. *42*, D92–D97.

Liu, Z., Pan, H.-M., Xin, L., Zhang, Y., Zhang, W.-M., Cao, P., and Xu, H.-W. (2019). Circ-ZNF609 promotes carcinogenesis of gastric cancer cells by inhibiting miRNA-145-5p expression. Eur. Rev. Med. Pharmacol. Sci. *23*, 9411–9417.

Liu, Z., Liu, F., Wang, F., Yang, X., and Guo, W. (2021). CircZNF609 promotes cell proliferation, migration, invasion, and glycolysis in nasopharyngeal carcinoma through regulating HRAS via miR-338-3p. Mol. Cell. Biochem. *476*, 175–186.

López de Silanes, I., Fan, J., Yang, X., Zonderman, A.B., Potapova, O., Pizer, E.S., and Gorospe, M. (2003). Role of the RNA-binding protein HuR in colon carcinogenesis. Oncogene *22*, 7146–7154.

Mann, M., Wright, P.R., and Backofen, R. (2017). IntaRNA 2.0: enhanced and customizable prediction of RNA-RNA interactions. Nucleic Acids Res. *45* (W1), W435–W439.

Martone, J., Mariani, D., Santini, T., Setti, A., Shamloo, S., Colantoni, A., Capparelli, F., Paiardini, A., Dimartino, D., Morlando, M., and Bozzoni, I. (2020). SMaRT lncRNA controls translation of a G-quadruplex-containing mRNA antagonizing the DHX36 helicase. EMBO Rep. *21*, e49942.

Mazan-Mamczarz, K., Galbán, S., de Silanes, I.L., Martindale, J.L., Atasoy, U., Keene, J.D., and Gorospe, M. (2003). RNA-binding protein HuR enhances p53 translation in response to ultraviolet light irradiation. Proc. Natl. Acad. Sci. USA *100*, 8354–8359.

Mazan-Mamczarz, K., Hagner, P.R., Corl, S., Srikantan, S., Wood, W.H., Becker, K.G., Gorospe, M., Keene, J.D., Levenson, A.S., and Gartenhaus, R.B. (2008). Post-transcriptional gene regulation by HuR promotes a more tumorigenic phenotype. Oncogene *27*, 6151–6163.

Memczak, S., Jens, M., Elefsinioti, A., Torti, F., Krueger, J., Rybak, A., Maier, L., Mackowiak, S.D., Gregersen, L.H., Munschauer, M., et al. (2013). Circular RNAs are a large class of animal RNAs with regulatory potency. Nature *495*, 333–338.

Miller, M.P., Asbury, C.L., and Biggins, S. (2016). A TOG protein confers tension sensitivity to kinetochore-microtubule attachments. Cell *165*, 1428–1439.

Moore, A.T., Rankin, K.E., von Dassow, G., Peris, L., Wagenbach, M., Ovechkina, Y., Andrieux, A., Job, D., and Wordeman, L. (2005). MCAK associates with the tips of polymerizing microtubules. J. Cell Biol. *169*, 391–397.

Noh, J.H., Kim, K.M., Abdelmohsen, K., Yoon, J.-H., Panda, A.C., Munk, R., Kim, J., Curtis, J., Moad, C.A., Wohler, C.M., et al. (2016). HuR and GRSF1 modulate the nuclear export and mitochondrial localization of the lncRNA *RMRP*. Genes Dev. *30*, 1224–1239.

Noh, J.H., Kim, K.M., McClusky, W.G., Abdelmohsen, K., and Gorospe, M. (2018). Cytoplasmic functions of long noncoding RNAs. Wiley Interdiscip. Rev. RNA *9*, e1471.

Olive, P.L., and Banáth, J.P. (2006). The comet assay: A method to measure DNA damage in individual cells. Nat. Protoc. *1*, 23–29.

Panda, S.P., Chinnaswamy, G., Vora, T., Prasad, M., Bansal, D., Kapoor, G., Radhakrishnan, V., Agarwala, S., Laskar, S., Arora, B., et al. (2017). Diagnosis and management of rhabdomyosarcoma in children and adolescents: ICMR consensus document. Indian J. Pediatr. *84*, 393–402.

Patop, I.L., and Kadener, S. (2018). circRNAs in Cancer. Curr. Opin. Genet. Dev. *48*, 121–127.

Quinlan, A.R., and Hall, I.M. (2010). BEDTools: a flexible suite of utilities for comparing genomic features. Bioinformatics *26*, 841–842.

Rosa, A., Papaioannou, M.D., Krzyspiak, J.E., and Brivanlou, A.H. (2014). miR-373 is regulated by TGFβ signaling and promotes mesendoderm differentiation in human Embryonic Stem Cells. Dev. Biol. *391*, 81–88.

Rossi, F., Legnini, I., Megiorni, F., Colantoni, A., Santini, T., Morlando, M., Di Timoteo, G., Dattilo, D., Dominici, C., and Bozzoni, I. (2019). Circ-ZNF609 regulates G1-S progression in rhabdomyosarcoma. Oncogene *38*, 3843–3854.

Salzman, J. (2016). Circular RNA expression: Its potential regulation and function. Trends Genet. *32*, 309–316.

Sanz, E., Yang, L., Su, T., Morris, D.R., McKnight, G.S., and Amieux, P.S. (2009). Cell-type-specific isolation of ribosome-associated mRNA from complex tissues. Proc. Natl. Acad. Sci. USA *106*, 13939–13944.

Sousa Martins, J.P., Liu, X., Oke, A., Arora, R., Franciosi, F., Viville, S., Laird, D.J., Fung, J.C., and Conti, M. (2016). DAZL and CPEB1 regulate mRNA translation synergistically during oocyte maturation. J. Cell Sci. *129*, 1271–1282.

Srikantan, S., and Gorospe, M. (2012). HuR function in disease. Front. Biosci. *17*, 189–205.

Statello, L., Guo, C.-J., Chen, L.-L., and Huarte, M. (2021). Gene regulation by long non-coding RNAs and its biological functions. Nat. Rev. Mol. Cell Biol. *22*, 96–118.

Stingele, S., Stoehr, G., Peplowska, K., Cox, J., Mann, M., and Storchova, Z. (2012). Global analysis of genome, transcriptome and proteome reveals the response to aneuploidy in human cells. Mol. Syst. Biol. *8*, 608.

Thawani, A., Kadzik, R.S., and Petry, S. (2018). XMAP215 is a microtubule nucleation factor that functions synergistically with the γ-tubulin ring complex. Nat. Cell Biol. *20*, 575–585.

Torosantucci, L., De Luca, M., Guarguaglini, G., Lavia, P., and Degrassi, F. (2008). Localized RanGTP accumulation promotes microtubule nucleation at kinetochores in somatic mammalian cells. Mol. Biol. Cell *19*, 1873–1882.

Uren, P.J., Bahrami-Samani, E., Burns, S.C., Qiao, M., Karginov, F.V., Hodges, E., Hannon, G.J., Sanford, J.R., Penalva, L.O.F., and Smith, A.D. (2012). Site identification in high-throughput RNA-protein interaction data. Bioinformatics *28*, 3013–3020.

Vasquez, R.J., Howell, B., Yvon, A.M., Wadsworth, P., and Cassimeris, L. (1997). Nanomolar concentrations of nocodazole alter microtubule dynamic instability in vivo and in vitro. Mol. Biol. Cell *8*, 973–985.

Verrico, A., Rovella, P., Di Francesco, L., Damizia, M., Staid, D.S., Le Pera, L., Schininà, M.E., and Lavia, P. (2020). Importin-β/karyopherin-β1 modulates mitotic microtubule function and taxane sensitivity in cancer cells via its nucleoporin-binding region. Oncogene *39*, 454–468.

Wang, W., Caldwell, M.C., Lin, S., Furneaux, H., and Gorospe, M. (2000). HuR regulates cyclin A and cyclin B1 mRNA stability during cell proliferation. EMBO J. *19*, 2340–2350.

Wang, S., Xue, X., Wang, R., Li, X., Li, Q., Wang, Y., Xie, P., Kang, Y., Meng, R., and Feng, X. (2018). CircZNF609 promotes breast cancer cell growth, migration, and invasion by elevating p70S6K1 via sponging miR-145-5p. Cancer Manag. Res. *10*, 3881–3890.

Wang, F., Zuroske, T., and Watts, J.K. (2020). RNA therapeutics on the rise. Nat. Rev. Drug Discov. *19*, 441–442.

CellPress
OPEN ACCESS

Wein, G., Rössler, M., Klug, R., and Herget, T. (2003). The 3′-UTR of the mRNA coding for the major protein kinase C substrate MARCKS contains a novel CU-rich element interacting with the mRNA stabilizing factors HuD and HuR. Eur. J. Biochem. *270*, 350–365.

Williams, B.R., Prabhu, V.R., Hunter, K.E., Glazier, C.M., Whittaker, C.A., Housman, D.E., and Amon, A. (2008). Aneuploidy affects proliferation and spontaneous immortalization in mammalian cells. Science *322*, 703–709.

Wu, X., Lan, L., Wilson, D.M., Marquez, R.T., Tsao, W.C., Gao, P., Roy, A., Turner, B.A., McDonald, P., Tunge, J.A., et al. (2015). Identification and validation of novel small molecule disruptors of HuR-mRNA interaction. ACS Chem. Biol. *10*, 1476–1484.

Wu, W., Wei, N., Shao, G., Jiang, C., Zhang, S., and Wang, L. (2019). circZNF609 promotes the proliferation and migration of gastric cancer by sponging miR-483-3p and regulating CDK6. OncoTargets Ther. *12*, 8197–8205.

Yeap, B.B., Voon, D.C., Vivian, J.P., McCulloch, R.K., Thomson, A.M., Giles, K.M., Czyzyk-Krzeska, M.F., Furneaux, H., Wilce, M.C.J., Wilce, J.A., et al. (2002). Novel binding of HuR and poly(C)-binding protein to a conserved UC-rich motif within the 3′-untranslated region of the androgen receptor messenger RNA. J. Biol. Chem. *277*, 27183–27192.

Zerbino, D.R., Achuthan, P., Akanni, W., Amode, M.R., Barrell, D., Bhai, J., Billis, K., Cummins, C., Gall, A., Girón, C.G., et al. (2018). Ensembl 2018. Nucleic Acids Res. *46* (D1), D754–D761.

Zhu, L., Liu, Y., Yang, Y., Mao, X.-M., and Yin, Z.-D. (2019). CircRNA ZNF609 promotes growth and metastasis of nasopharyngeal carcinoma by competing with microRNA-150-5p. Eur. Rev. Med. Pharmacol. Sci. *23*, 2817–2826.

STAR★METHODS

KEY RESOURCES TABLE

REAGENT or RESOURCE	SOURCE	IDENTIFIER
Antibodies		
Rabbit polyclonal anti-α-Actinin (H-300)	Santa Cruz Biotechnology	Cat#sc-15335; RRID: AB_2223809
Mouse monoclonal anti-β-Actin-Peroxidase (clone AC-15)	Sigma-Aldrich	Cat#A3854; RRID: AB_262011
Rabbit polyclonal anti-ch-TOG (CKAP5)	Bethyl	Cat#A301-971A; RRID: AB_1547921
Rabbit polyclonal anti-Srrm1	Novus Biologicals	Cat#NBP2-13381
Mouse monoclonal anti-Rent2 (UPF2) (G-10)	Santa Cruz Biotechnology	Cat#sc-374230; RRID: AB_10988267
Mouse monoclonal anti-Elavl1	Santa Cruz Biotechnology	Cat#sc-5261; RRID: AB_627770
Rabbit polyclonal anti-Ddx27	Proteintech	Cat#17087-1-AP; RRID: AB_2092569
Mouse monoclonal anti-p-Histone H2A.X Antibody (Ser 139)	Santa Cruz Biotechnology	Cat#sc-517348; RRID: AB_2783871
Mouse monoclonal anti-Gapdh (4F8), HRP Conjugated	Bioss Antibodies	Cat#bsm-33033M-HRP
Rabbit polyclonal anti-β-Catenin	Bethyl	Cat#A302-012A; RRID: AB_1576496
Mouse monoclonal anti-Flag M2	Sigma-Aldrich	Cat#F1804; RRID: AB_259529
Monoclonal anti-Flag M2-Peroxidase (HRP)	Sigma-Aldrich	Cat#A8592; RRID: AB_439702
Mouse monoclonal anti-α-Tubulin (clone B-5-1-2)	Sigma-Aldrich	Cat#T5168; RRID: AB_477579
Goat anti-rabbit IgG	Invitrogen	Cat#A1008
Donkey anti-mouse IgG	Invitrogen	Cat#A32787; RRID: AB_2762830
Goat polyclonal anti-Mouse IgG (H+L) Cross-Adsorbed Secondary Antibody, Alexa Fluor 488	ThermoFisher Scientific	Cat#A-11001; RRID: AB_2534069
Rhodamine Red-X AffiniPure F(ab')$_2$ Fragment Goat Anti-Mouse IgG (H+L) Secondary antibody	Jackson Immunology	Cat#115-296-003; RRID: AB_2338774
Bacterial and virus strains		
Subcloning efficiency DH5α competent cells	ThermoFisher Scientific	Cat#18265017
Chemicals, peptides, and recombinant proteins		
DMEM high-glucose	Sigma-Aldrich	Cat#D6546
FBS	Sigma-Aldrich	Cat#F7524
L-glutamine	Sigma-Aldrich	Cat#G7513
Penicillin-streptomycin	Sigma-Aldrich	Cat#P0781
RPMI 1640	ThermoFisher Scientific	Cat#11875085
Sodium pyruvate	ThermoFisher Scientific	Cat#11360070
GlutaMAX Supplement	ThermoFisher Scientific	Cat#35050061
Doxycycline hyclate	Sigma-Aldrich	Cat#D9891
Dharmafect-1 Transfection Reagent	Dharmacon	Cat#T-2001-02
Lipofectamine 2000	ThermoFisher Scientific	Cat#11668019
Opti-MEM Reduced Serum Medium	ThermoFisher Scientific	Cat#31985070
Puromycin	SERVA	Cat# 33835.02
TET-free FBS	Euro Clone	Cat#ECS0182L
cOmplete, EDTA-free PIC	Roche-Merck	Cat#11873580001

(*Continued on next page*)

Continued

REAGENT or RESOURCE	SOURCE	IDENTIFIER
WesternBright ECL Chemiluminescent HRP Substrate	Advansta	Cat#K-12045
Clarity Max Western ECL Substrate	Bio-Rad	Cat#1705062
Qiazol reagent	QIAGEN	Cat#79306
PrimeScript RT Reagent Kit	TakaraBio	Cat#RR037B
SuperScript VILO cDNA Synthesis Kit	ThermoFisher Scientific	Cat#11754050
PowerUp SYBR Green Master Mix	ThermoFisher Scientific	Cat#A25742
CloneAmp HiFi PCR Premix	Clontech	Cat#639298
4′-Aminomethyl-4,5′,8-trimethylpsoralen hydrochloride	Sigma-Aldrich	Cat#A4330
Proteinase K	Ambion	Cat#AM2548
RiboLock RNase Inhibitor	ThermoFisher Scientific	Cat#EO0384
Streptavidin MagneSphere paramagnetic particles	Promega	Cat#Z5481
Anti-FLAG M2 magnetic beads	Sigma-Aldrich	Cat#M8823
Dynabeads protein G	ThermoFisher Scientific	Cat#10003D
Vincristine	Selleckchem	Cat#S1241
Taxol (Paclitaxel)	Selleckchem	Cat#S1150
Nocodazole	Sigma-Aldrich	Cat#M1404
Crystal violet solution	Sigma-Aldrich	Cat#C0775
Trypan blue solution	ThermoFisher Scientific	Cat#15250061
Actinomycin D	Sigma-Aldrich	Cat#A9415-5MG
HuR-ARE Interaction Inhibitor, CMLD-2	Sigma-Aldrich	Cat# 5.38339
UltraPure Ethidium Bromide	ThermoFisher Scientific	Cat#15585011
Collagen I, Rat Tail	Corning	Cat#354236
DAPI solution	Sigma-Aldrich	Cat#D9542
ProLong Diamond Antifade Mountant	ThermoFisher Scientific	Cat#P36961
Critical commercial assays		
In-Fusion HD Cloning Kit	Clontech	Cat#639650
Direct-zol RNA Miniprep kit	Zymo Research	Cat#R2050
Deposited data		
CircZNF609 AMT-crosslinked pull-down (raw data)	This paper	GEO: GSE174172
ELAVL1 PAR-CLIP	Lebedeva et al., 2011	GEO: GSE29943
ELAVL1 PAR-CLIP	Kishore et al., 2011	GEO: GSE28859
miRNAs expression in rhabdomyosarcoma cells	Bersani et al., 2016	SRA: PRJNA326118
Experimental models: Cell lines		
Human: RD cells	ATCC	Cat#CCL-136; RRID: CVCL_1649
Human: SK-N-BE cells	ATCC	Cat#CRL-2271; RRID: CVCL_0528
Human: K562 cells	ATCC	Cat#CCL-243; RRID: CVCL_0004
Experimental models: Organisms/strains		
Mouse: Crl:CD1-Foxn1^{nu} (CD-1 Nude)	Charles River Laboratories	Strain 086
Oligonucleotides		
DNA oligonucleotides for qRT-PCR/PCR experiments used in this work are listed in Table S2	This paper	N/A
Biotinylated DNA probes used in this work are listed in Table S2	This paper	N/A

(*Continued on next page*)

Continued

REAGENT or RESOURCE	SOURCE	IDENTIFIER
DNA blocker oligonucleotides used in this work are listed in Table S2	This paper	N/A
LNA-modified oligonucleotides used in this work are listed in Table S2	This paper	N/A
siRNAs used in this work are listed in Table S2	This paper	N/A
Recombinant DNA		
pSuperioir-GFP-pTRE3G-TetOn3g_shRNAZNF609-03-PGK-EGFP-IRES-Zeo vector	Prof Gunter Meister's Lab	N/A
Enhanced PiggyBac Transposable Vector (epB-Puro-TT)	Prof Alessandro Rosa's Lab (Rosa et al., 2014)	N/A
ePB-PuroTT-shRNA-C vector	This paper	N/A
Transposase-expressing Helper construct	Prof Alessandro Rosa's Lab	N/A
RPL22 (Myc-DDK-tagged)-Human ribosomal protein L22	Origene	Cat#RC208910
pcDNA 3.1^{+} Mammalian Expression Vector	ThermoFisher Scientific	Cat#V79020
GFP-Tog vector	Moore et al., 2005	Addgene #29480
p-CKAP5-FLAG-3′WT	This paper	N/A
p-CKAP5-FLAG-3′Δ	This paper	N/A
Software and algorithms		
Image Lab	Bio-Rad	https://www.bio-rad.com/it-it/product/image-lab-software?ID=KRE6P5E8Z
IGV (Integrative Genomics Viewer)	Broad Institute and the Regents of the University of California	https://software.broadinstitute.org/software/igv/download
ImageJ	NIH	https://imagej.nih.gov/ij/download.html
ImageJ Macro "Comet Assay"	Robert Bagnell, Pathology & Lab Med UNC-CH	https://www.med.unc.edu/microscopy/resources/imagej-plugins-and-macros/comet-assay/
NIS-Elements AR 3.2	Nikon	NIS Nikon proprietary software https://www.microscope.healthcare.nikon.com/en_EU/products/software/nis-elements/nis-elements-advanced-research https://nis-elements-viewer.software.informer.com/3.2; available at https://www.imagingplatformibpmcnr.it/
NIS-Element AR 5.02	Nikon	Nikon proprietary software https://www.microscope.healthcare.nikon.com/en_EU/products/software/nis-elements/nis-elements-advanced-research https://www.nikon.com/products/microscope-solutions/support/download/software/imgsfw/nis-d_v5020364.htm available at https://www.imagingplatformibpmcnr.it/
Trimmomatic version 0.32	Bolger et al., 2014	http://www.usadellab.org/cms/?page=trimmomatic
STAR aligner version 2.5.2b	Dobin et al., 2013	https://github.com/alexdobin/STAR

(*Continued on next page*)

Continued

REAGENT or RESOURCE	SOURCE	IDENTIFIER
BEDTools version 2.21.0	Quinlan and Hall, 2010	https://github.com/arq5x/bedtools2
Picard version 2.18.23	Broad Institute	https://broadinstitute.github.io/picard/
BamTools version 2.3.0	Barnett et al., 2011	https://github.com/pezmaster31/bamtools/
SAMtools version 1.9	Li et al., 2009	http://www.htslib.org/download/
Piranha version 1.2.1	Uren et al., 2012	http://smithlabresearch.org/software/piranha/
IntaRNA version 2.4.1	Freiburg RNA Tools (Mann et al., 2017)	http://rna.informatik.uni-freiburg.de/IntaRNA/Input.jsp
starBase 2.0	Li et al., 2014	https://starbase.sysu.edu.cn/starbase2/index.php

RESOURCE AVAILABILITY

Lead contact

Further information and requests for resources and reagents should be directed to and will be fulfilled by the lead contact, Irene Bozzoni (irene.bozzoni@uniroma1.it).

Materials availability

All unique/stable reagents generated in this study are available from the lead contact upon request.

Data and code availability

- RNA-sequencing data from RNA pull-down experiments have been deposited at Gene Expression Omnibus (GEO) and are publicly available as of the date of publication with accession code GEO: GSE174172. The accession number is listed in the Key resources table.
- This paper refers to publicly available data. These accession numbers for the datasets are listed in the Key resources table.
- All software used in this manuscript are listed in the Key resources table.
- This paper does not report original code.
- Any additional information required to reanalyze the data reported in this paper is available from the lead contact upon request.

EXPERIMENTAL MODEL AND SUBJECT DETAILS

Cell cultures

All cell lines used in this study were grown at 37°C, 5% CO_2. All cell lines were tested for mycoplasma contamination.

Human RD cells (embryonal rhabdomyosarcoma cell line derived from a female patient) were cultured in DMEM high-glucose supplemented with 10% fetal bovine serum (FBS), 2 mM L-glutamine and 1% penicillin-streptomycin.

Human SK-N-BE cells (neuroblastoma cell line derived from a male patient) were cultured in RPMI 1640 medium supplemented with 10% FBS, 1% sodium pyruvate, 1% glutamax and 1% penicillin-streptomycin.

Human K562 cells (chronic myelogenous leukemia cell line derived from a female patient) were cultured in RPMI 1640 medium supplemented with 10% heat-inactivated FBS, 2 mM L-glutamine and 1% penicillin-streptomycin.

Xenograft mice establishment and tumor measurements

$5x10^6$ stable RD cells expressing the doxycycline-inducible shRNA targeting circZNF609 were subcutaneously injected in the scapular region of 10 4-week-old female CD-1 nude mice (Charles River Laboratories). Mice were then randomly divided into two groups kept in two different cages, one receiving drinking water supplemented with 1 mg/ml doxycycline (doxycycline hyclate, Sigma-Aldrich) + 3% (v/v) sucrose, the other receiving drinking water supplemented with only 3% (v/v) sucrose. Supplemented drinking water was replaced every two days. As soon as the tumor masses appeared, their length (L) and width (W) were measured with a caliper three times a week. Tumor volume calculations were obtained using the formula (W^2xL)/2. Mice were sacrificed by cervical dislocation when their tumor's largest dimension reached 20 mm. Then, the tumors were surgically removed and snap-frozen in liquid nitrogen. RNA was extracted from the tissue and circZNF609 and *GAPDH* mRNA levels were measured by qRT-PCR, as described below. Mice were then re-grouped based on circZNF609 expression level, putting the cut-off at 0.0025 (= ΔΔCt of circZNF609 relative to *GAPDH* mRNA). One mouse in the doxycycline-treated group died unexpectedly and was therefore removed from the analysis. Another mouse from the doxycycline-treated group and a mouse from the doxycycline-untreated group were also removed from

the analysis because of experimental issues. All the procedures involving animals and their care were approved by the Italian Ministry of Health (Prot. 18/2015-UT) and were conformed to the relevant regulatory standards in accordance with the Italian legislation.

METHOD DETAILS

Plasmid construction

RPL22 (Myc-DDK-tagged) plasmid was purchased from Origene, and we referred to it as the RPL22-FLAG plasmid.

The p-CKAP5-FLAG-3′WT and p-CKAP5-FLAG-3′Δ vectors were obtained starting from the GFP-Tog plasmid (Addgene #29480; Moore et al., 2005). Briefly, the GFP-tag downstream the CKAP5 coding sequence in GFP-Tog vector was removed by inverse PCR using ΔGFP oligonucleotides. Wild-type *CKAP5* 3′UTR sequence (nucleotides 1-505 of the 3′UTR sequence) preceded by the 3xFLAG-coding sequence (5'GACTACAAAGACCATGACGGTGATTATAAAGATCATGACATCGATTACAAGGATGACGATGACAAG3') was PCR-amplified from a plasmid already available in our laboratory using 3XFLAG_CKAP5-3′UTR oligonucleotides. The wild-type 3XFLAG-*CKAP5* 3′UTR insert was then cloned into the CKAP5 coding sequence-containing plasmid using the In-Fusion HD Cloning Kit (Clontech). To add *CKAP5* 5′UTR sequence upstream the CKAP5 coding sequence, the previously obtained vector was opened by inverse PCR using CKAP5-5′UTR_inverse-PCR oligonucleotides, while the insert with the *CKAP5* 5′UTR sequence was obtained by annealing the two CKAP5-5′UTR _insert complementary oligonucleotides. The two DNA pieces were then cloned together using the In-Fusion HD Cloning Kit, obtaining the p-CKAP5-FLAG-3′WT plasmid. To obtain the p-CKAP5-FLAG-3′Δ plasmid, the sequence interacting with circZNF609 BSJ in *CKAP5* 3′UTR was removed by inverse PCR using 5′-phosphorylated Δ_circ oligonucleotides, and then the final plasmid was obtained by self-ligation of the PCR product.

To obtain the ePB-PuroTT-shRNA-C vector to establish the stable RD cell line expressing the inducible shRNA targeting circZNF609 (shRNA-C has the same sequence as the si-Circ described in Table S2), the miR-331-precursor/sh-Circ cassette was amplified from the pSuperioir-GFP-pTRE3G-TetOn3g_shRNAZNF609-03-PGK-EGFP-IRES-Zeo vector kindly provided by Prof Gunter Meister's Lab, using ZNF609shRNA-cassette oligonucleotides. This cassette was cloned into a HindIII/NotI digested Enhanced PiggyBac Transposable Vector (epB-Puro-TT [Rosa et al., 2014], kindly provided by Prof Alessandro Rosa's Lab) using the In-Fusion HD Cloning Kit, obtaining the final plasmid.

The transposase-expressing Helper vector was kindly provided by Prof Alessandro Rosa's Lab.

CloneAmp HiFi PCR Premix (Clontech) was used to perform all the PCR reactions needed to obtain these plasmids, according to the manufacturer's instructions. All the oligonucleotides used for cloning are listed in Table S2.

Cell transfection

For siRNA (ON-TARGETplus, Dharmacon) transfections, either 30 nM of si-Circ, si-

Circ+Lin, si-Lin, si-CKAP5 or 30, 60 or 90 nM of si-ELAVL1, and the corresponding concentration of si-SCR, were transfected with Dharmafect-1 Transfection Reagent (Dharmacon), according to the manufacturer's instructions. Unless differentially specified, the medium was replaced 24 h after transfection and cells were harvested after another 24 h. siRNAs used in this work are listed in Table S2.

For LNA-modified oligonucleotide (IDT-Integrated DNA Technologies) transfections, 7.5 nM of LNA-modified oligonucleotides were transfected with Dharmafect-1 Transfection Reagent according to manufacturer's instructions, unless differentially specified. Medium was replaced 24 h after the transfection and cells were split in a 1:5 ratio 48 h after transfection and harvested after another 24h, unless differentially specified. Sequences of LNA-modified oligonucleotides used in this work are listed in Table S2. LNA SCR was designed to target the synthetic firefly luciferase gene hluc+, with a 2-nt mutation to abolish a secondary structure in the oligonucleotide. LNAs BSJ (1 and 2), LNA Ex2, and LNAs on ELAVL1 sites (1, 2 and 3) target different regions on circZNF609. LNAs *CKAP5* (1 and 2) target *CKAP5* mRNA 3′UTR at the level of the predicted interaction with circZNF609 BSJ.

Plasmid DNA transfections were performed using Lipofectamine 2000 (ThermoFisher Scientific), according to the manufacturer's instructions.

To achieve CKAP5-FLAG overexpression, 500 ng of p-CKAP5-FLAG-3′WT or p-CKAP5-FLAG-3′Δ vector were added to 75 μL Opti-MEM reduced serum medium (ThermoFisher Scientific), and 1.5 μL Lipofectamine 2000 were added to other 75 μL Opti-MEM separately. The two mixtures were briefly vortexed and left 5 min at room temperature, then they were mixed and after another 10 min at room temperature they were added to cells in 1 mL fresh medium. Medium was replaced 6 h after transfection and cells were harvested 48 h after transfection. When CKAP5-FLAG overexpression was coupled with si-SCR and si-Circ transfection, RD cells were transfected with 30 nM siRNAs as previously described. 6 h after siRNA transfection, p-CKAP5-FLAG-3′WT plasmid was transfected as described before. Cells were harvested 48 h after plasmid transfection.

Detailed information about the amount of DNA used for transfecting other plasmids used in this work are provided in the following sections.

Establishment of an RD cell line expressing a circZNF609-targeting shRNA

To establish a stable RD cell line expressing an shRNA targeting circZNF609, $5x10^5$ RD cells were plated in a 6-cm culture dish. 12 h after the plating, culture medium was replaced and the ePB-PuroTT-shRNA-C vector and the transposase-expressing Helper construct were transfected in a 4:1 ratio with Lipofectamine 2000 and Opti-MEM, according to the manufacturer's protocol. 12 h after

transfection, culture medium was replaced and, after another 12 h, culture medium was replaced and supplemented with 1 μg/ml puromycin to select transfected cells in which the transposon was integrated. After selection, stable RD cells were switched to a puromycin-free, TET-free culture medium, and the shRNA inducible expression was tested by culturing cells with doxycycline.

Actinomycin D cell treatment for RNA analysis

Cells in 6-cm plates were transfected with either si-SCR or si-Circ as previously described. 24 h after transfection, an equal number of si-SCR- and si-Circ-transfected cells were plated into five 35-mm plates, respectively. 48 h after transfection, one plate si-SCR and one plate si-Circ were harvested (0 h). For both the si-SCR and si-Circ sets, fresh medium was replaced to three plates and supplemented with Actinomycin D (5 μg/ml in DMSO, Sigma-Aldrich), while fresh medium supplemented with an equal volume of 100% DMSO was added to the remaining plate. Actinomycin D-treated cells were harvested after 2.5 h, 5 h and 7.5 h of treatment, while DMSO-treated cells were harvested after 7.5 h of treatment. An equal quantity of RNA extracted from Actinomycin D- or DMSO-treated cells at each time-point was used for the reverse transcription reaction. Graphs represent fold changes calculated as $2^{-\Delta Ct}$, normalized to the reference sample (0 h) which was set as 1. DMSO-treated cells were used to control mRNA stability in each condition.

CMLD-2 cell treatment for protein analysis

$5x10^4$ RD cells were plated in a 12-well plate and either 30 μM CMLD-2 HuR-ARE Interaction Inhibitor (Sigma-Aldrich) or an equal volume of 100% DMSO was immediately added to the medium. Fresh CMLD-2- or DMSO-supplemented medium was replaced every 24 h. Cells were harvested 96 h after plating and then prepared for protein analysis. An equal quantity of proteins extracted from CMLD-2- or DMSO-treated cells was loaded on a polyacrylamide gel to be analyzed by western blot.

Microtubule-targeting drug cell treatments

RD and K562 cells were transfected with either siRNAs or LNA-modified oligonucleotides as previously described. 24 h after transfection, an equal number of transfected live cells were plated into a 12-well plate. At the same time, the indicated concentrations of either Vincristine (Selleckchem), Taxol (Paclitaxel - Selleckchem) or Nocodazole (Sigma) were added to the medium.

SK-N-BE cells were transfected with either si-SCR or si-Circ as previously described.

24 h after transfection cells were plated in 96-well plates ($3x10^4$ cells/well), and the following day treated with the indicated concentrations of either Taxol or Vincristine.

24 h after the addition of the drugs, viable RD and SK-N-BE cells were stained with crystal violet solution (0.5%) and then the absorbance was read at 600 nm, using a Glomax-Multi+ Detection System machine (Promega). Instead, dead/live K562 cells were counted with the addition of 0.4% Trypan Blue stain (ThermoFisher Scientific) at a CytoSmart cell counter (Corning). Survival was expressed as percentage of cells alive normalized to DMSO-treated cells (vehicle control), and untreated cells were used to control each condition.

Western blot

Cells were harvested in a suitable volume of Protein Extraction Buffer (100 mM Tris pH 7.5, EDTA 1 mM, SDS 2%, PIC 1X (Complete-EDTA free, Roche–Merck), incubated 20 min on ice and centrifuged at 15000 x g for 15 min at 4°C. Proteins (5-10 μg for most of the experiments) were loaded on a 4%–12% bis-tris-acrylamide gel and transferred to a nitrocellulose membrane. The membrane was blocked in 5% milk and hybridized with the specific primary antibody for 1 h at room temperature or overnight at 4°C. If required, membrane was then hybridized with the appropriate secondary antibody (Invitrogen) for 1 h at room temperature. Protein detection was carried out with WesternBright® ECL Chemiluminescent HRP Substrate (Advansta) or with Clarity Max Western ECL Substrate (Bio-Rad). Images were acquired using a ChemiDoc MP Imager (Bio-Rad) and analyzed using Image Lab 5.2.1 software (Bio-Rad). Whole images were linearly adjusted in contrast and brightness when necessary.

RNA isolation and analysis

Total RNA was extracted with Qiazol reagent (QIAGEN) and Direct-zol RNA Miniprep kit (Zymo Research) with a 15-minute DNase-I treatment according to the manufacturer's protocol, unless differentially specified.

Reverse transcription reaction for routine experiments was performed using PrimeScript RT Reagent Kit (Takara Bio), while for RNA derived from RNA pull-down and RIP/CLIP experiments the SuperScript VILO cDNA Synthesis Kit (ThermoFisher Scientific) was used according to the manufacturer's protocol.

qRT-PCR was performed using PowerUp SYBR Green Master Mix reagent (ThermoFisher Scientific) according to the manufacturer's instructions. RNA levels are relative to *GAPDH* mRNA in routine experiments. Relative RNA quantity was calculated as the fold change ($2^{-\Delta\Delta Ct}$) with respect to the control sample set as 1, unless differently specified. A complete list of the oligonucleotides used for qRT-PCR experiments is provided in Table S2.

RNA pull-down

The psoralen-crosslinked RNA pull-down protocol was performed as described in Martone et al. (2020), with some modifications in the first steps. Briefly, $1x10^7$ RD cells for each biological replicate were pelleted, resuspended in 1 mL of ice-cold complete PBS

supplemented with 0.5 mg/ml of 4'-aminomethyl-4,5′,8-trimethylpsoralen (AMT, Sigma-Aldrich), and crosslinked at 365 nm for five 2-min cycles. 1 volume of Guanidinium Hydrochloride 6M was added to 1 volume of AMT. The lysate was subdivided into 250 μL aliquots. To each aliquot, 25 μL of a 20 mg/mL solution of Proteinase K (Ambion) and 6.5 μL of 20% SDS were added. The samples were then incubated at 65°C for 1 h. RNA was precipitated through phenol-chloroform extraction and the protocol proceeded as previously described. At the end of the experiment, the recovered RNA fraction was either used for qRT-PCR experiments or sent for total RNA-sequencing analysis (NovaSeq - Illumina) at IGA Technology Services (Udine, Italy). Ovation RNA v2 followed by Ovation Ultralow v2 kit was used to prepare cDNA libraries for pull-down RNA-Seq experiments. The sequencing reactions, performed on an Illumina NovaSeq 6000 Sequencing system, produced an average of 43.5 million 150-nucleotide long paired-end reads per sample.

For native RNA pull-down, $1x10^7$ RD cells per pull-down were lysed in a buffer containing Tris-HCl pH 7.5 50mM; NaCl 150 mM; $MgCl_2$ 3 mM; NP40 0.5%; EDTA 2 mM; DTT 1 mM plus protease inhibitors and RNase inhibitors. After lysis and clearing by centrifugation, samples were diluted in a 1:2 ratio with hybridization buffer containing Tris-HCl pH 7.5 100 mM, NaCl 300 mM, $MgCl_2$ 1 mM, SDS 0.2%, Formamide 15%, NP40 0.5%, EDTA 10 mM, DTT 1 mM plus protease inhibitors and RNase inhibitors. 100 pmol of previously heat-denaturated biotinylated probes were added. After a 4-h incubation at 4°C, 0.1 mL of streptavidin Magnasphere paramagnetic beads (Promega) were added to pull down the complex, and the mixture was incubated 1 h at room temperature. After pull-down, beads were washed 4 times with hybridization buffer and RNA was extracted by phenol-chloroform extraction.

When indicated, 400 pmol of previously denatured DNA oligo blocker was added to the probes to compete for the pull-down interactors.

Sequences of the biotinylated probes against circZNF609 or LacZ mRNA used in the RNA pull-down experiments and sequences of DNA blocker oligonucleotides are provided in Table S2.

RNA Immunoprecipitation assays

The RNA-immunoprecipitation (RIP) assays for ELAVL1 and RPL22-FLAG protein were performed in RD cells according to the protocol described in Keene et al. (2006).

To immunoprecipitate ELAVL1 in RD cells treated with either si-SCR or si-Circ, $2x10^6$ RD cells were plated in two 10-cm dishes and transfected with either 30 nM si-SCR or 30 nM si-Circ, respectively. Medium was replaced after 24 h and cells were harvested after another 24 h.

To immunoprecipitate ELAVL1 in RD cells treated with either LNA SCR or LNAs on ELAVL1 sites, $2x10^6$ RD cells were plated in two 10-cm dishes and transfected with either 100 nM LNA SCR or 100 nM LNAs on ELAVL1 sites (1+2+3), respectively. 24 h after transfection, cells in each 10-cm plate were moved to a separate 15-cm plate. Cells were harvested 72 h after transfection. ELAVL1 RIP assays were performed using Dynabeads Protein G (ThermoFisher Scientific) and anti-ELAVL1 (Santa Cruz Biotechnology) primary antibody.

To immunoprecipitate RPL22-FLAG in RD cells treated with either si-SCR or si-Circ, $2x10^6$ RD cells were plated in two 10-cm plates and transfected with either 10 μg pcDNA $3.1^{(+)}$ or 10 μg RPL22-FLAG plasmid, respectively. 8 h after transfection, both pcDNA- (empty) and RPL22-FLAG-transfected cells were split in a 1:2 ratio to two 10-cm plates. The following day, both pcDNA- and RPL22-FLAG-transfected cells were transfected with either 30 nM si-SCR or 30 nM si-Circ. 24 h after siRNA transfection, cells in each 10-cm plate were moved to a new 15-cm plate, and then harvested after another 24 h. Then RPL22-FLAG RIP assay was performed using anti-FLAG M2 magnetic beads (Sigma-Aldrich).

To immunoprecipitate RPL22-FLAG in RD cells treated with either DMSO or CDML-2, $2x10^6$ RD cells were plated in two 10-cm plates and either 30 μM CMLD-2 or an equal volume of 100% DMSO was added to the medium, respectively. The following day, CMLD-2- and DMSO-treated cells were transfected with RPL22-FLAG plasmid as described before, in supplemented medium. Cells were harvested 48 h after RPL22-FLAG transfection. Then RPL22-FLAG RIP assay was performed using Dynabeads Protein G and anti-FLAG M2 (Sigma-Aldrich) primary antibody.

Cross-linking immunoprecipitation (CLIP) was performed according to Beltran et al. (2019) with the following modifications. A total of $2.5x10^7$ RD cells per UV RNA immunoprecipitation (CLIP) were irradiated with 0.4 J/cm^2 of 254 nm UV light. Dynabeads Protein G were washed 3 times with wash buffer containing 500 mM NaCl, pelleted and then incubated in 200 μL PK buffer (100 mM Tris-HCl pH 7.4, 50 mM NaCl and 40 μL Proteinase K) for 20 min at 1100 rpm and 37°C. An equal volume of PK buffer containing 7 M urea was added, and a second incubation was performed. Supernatant was collected, and RNA was purified via phenol–chloroform extraction.

COMET assay

COMET assay was performed as described in Olive and Banáth (2006). Cell lysis and electrophoresis were performed in alkaline conditions. DNA was stained for 20 min at room temperature with 20 μL of a 10 mg/ml Ethidium Bromide solution (ThermoFisher Scientific) in 10 mL of distilled water; then slides were rinsed with distilled water to remove excess stain. Slides were imaged on a Zeiss AXIO Observer A1 microscope. Comet tail moment was measured using the ImageJ Macro "Comet Assay." Four independent biological replicates of this experiment were performed, three of them at 48 h after transfection and one at 72 h after transfection. Since the results were comparable, the data from the four experiments are shown all together.

Immunofluorescence

Cells were cultured on pre-coated glass coverslips (0.4 mg/ml Collagen Rat Tail, Corning), and then fixed in 4% paraformaldehyde in PBS for 20 min at 4°C. Cells were permeabilized in Triton 0.01% 15 min at room temperature, then blocked with 1% goat serum/PBS for 15 min at room temperature.

For the analysis of the damaged DNA marker, anti-gH2AX Ser139 primary antibody (Santa Cruz Biotechnology) was diluted 1:200 in 1% goat serum/PBS and incubated on the cells overnight at 4°C. Fluorescent goat anti-mouse IgG (H+L) cross-adsorbed secondary antibody (Alexa Fluor 488; ThermoFisher Scientific) was diluted 1:200 in 1% goat serum/PBS and incubated for 45 min at room temperature. After extensive washings with PBS, cells were incubated with DAPI solution (1 μg/ml/PBS; Sigma-Aldrich) for 5 min at room temperature, and then mounted using ProLong Diamond Antifade Mountant (ThermoFischer Scientific). Images were processed only in intensity threshold, contrast, and brightness on ImageJ software.

For the analyses of mitotic figures, cell samples were fixed in absolute MetOH (7 min, −20°C), washed twice in 1x PBS and blocked with 3% BSA/PBS-T (1 h, room temperature). Primary antibody to alpha-tubulin (Sigma-Aldrich) was diluted 1:1500 in 3% BSA/PBS-T and incubated for 1h at room temperature. Fluorescent secondary antibody conjugated to Rhodamine (Jackson Immunology) was diluted 1:50 in 3% BSA/PBS-T and incubated for 30 min at room temperature. The DNA was stained with 0.1 μg/ml DAPI solution.

Microtubule de-polymerization and re-polymerization assays and analysis of mitotic phenotypes

The protocols used for microtubule (MT) de-/re-polymerization assays and immunostaining were previously described in Torosantucci et al. (2008) and Verrico et al. (2020). Briefly, for MT de-polymerization assays, the cultures were placed on ice for 20 min, then washed twice in PTEMF buffer (20 mM PIPES, 10 mM EGTA, 1 mM $MgCl_2$ in dH_2O) to preserve resistant MTs, fixed (3.7% paraformaldehyde, 0.2% Triton X-100 in PTEMF) and finally processed for immunofluorescence to alpha-tubulin as above. At least 200 mitotic cells were analyzed in the experiment shown in Figure 5A.

For MT regrowth studies, the time of incubation in ice was prolonged to 40 min to obtain complete MT depolymerization, then immediately followed by incubation at 37°C for 30 s, 1 min, 2 min and 4 min. The cultures were then fixed and processed for immunofluorescence as described above. At least 300 mitotic cells/sample were analyzed in the experiment shown in Figure 5B.

For the analysis of frequently occurring mitotic abnormalities shown in Figure 5C, at least 190 cells were analyzed.

Fixed samples were analyzed under a Nikon Eclipse 90i microscope equipped with a Qicam Fast 1394 CCD camera (Qimaging); single cell analysis was performed using an immersion oil 100x objective (NA 1.3) and entire fields were scored under 40x objective (NA 0.75). The images were acquired using the NIS-Elements AR 3.2 software (Nikon). 3D deconvolution (0.4 μm z-serial optical sections) was performed using the ''AutoQuant'' deconvolution module of NIS-Element AR 5.02. Image projections were created from z stacks using the Maximum Intensity Projection (MIP) functions of NIS-Element AR 5.02.

RNA-Sequencing bioinformatic analyses

Adaptor sequences and poor quality bases were removed from raw reads using Trimmomatic software version 0.32 (Bolger et al., 2014) with parameters ILLUMINACLIP:path/to/adaptor:2:30:10:8:true LEADING:3 TRAILING:3 SLIDINGWINDOW:4:15 MINLEN:18. Alignment to human GRCh38 genome and Ensembl 90 transcriptome (Zerbino et al., 2018) was performed using STAR aligner version 2.5.2b (Dobin et al., 2013) with parameters–outFilterIntronMotifs RemoveNoncanonical–outSAMstrandField intronMotif–outSAMtype BAM SortedByCoordinate–outFilterType BySJout–outFilterMultimapNmax 20–alignSJoverhangMin 8–alignSJDBoverhangMin 1–outFilterMismatchNmax 999. Alignment files were further processed by filtering out reads mapping to rRNAs and tRNAs using BEDTools version 2.21.0 intersect tool (Quinlan and Hall, 2010), removing PCR duplicates using the MarkDuplicates tool included in the Picard suite version 2.18.23 and discarding the multi-mapped reads using BamTools version 2.3.0 (Barnett et al., 2011). Properly paired reads were extracted using SAMtools version 1.9 (Li et al., 2009). GRCh38 genome was divided into 170 bp long non-overlapping bins using the BEDtools makewindows tool. Properly paired fragments falling in each bin were counted using the BEDtools intersect tool; this way, sample-specific count files were created. Such files were given as input to Piranha version 1.2.1 (Uren et al., 2012) to call peaks for ODD and EVEN circZNF609 pull-down samples and LacZ pull-down sample, using Input sample counts as a covariate. Piranha parameters were set to -x -c -s. ODD peaks overlapping EVEN peaks were identified using the BEDtools intersect tool. Normalized coverage was calculated for such overlapping peaks in each sample, by dividing fragment counts by the total number of mapping fragments. Peaks where both ODD and EVEN coverages were at least four-fold higher than both Input and LacZ coverages were selected as circZNF609 pull-down enriched regions. BEDtools intersect tool was used to annotate such regions based on their overlap with Ensembl 90 exons and to filter out transcripts hosting LacZ peaks.

Prediction of RNA-RNA interacting regions

IntaRNA version 2.4.1 (Mann et al., 2017) was used to predict the binding regions between circZNF609 and the interactors found in the pull-down experiment. Since the tool does not natively handle circular RNA molecules, we used both the exonic circZNF609 sequence and the same sequence extended using its first 150 nucleotides, to also include the region around the back-splicing junction (BSJ). Except for *CKAP5* mRNA, the interacting regions identified in the examined targets when using the not extended circZNF609 sequence were the same as those found using the BSJ-extended sequence.

miRNA analysis

For miRNA analysis, miRNAs expressed in RD were extracted from Bersani et al. (2016) and prediction of miRNAs interacting with *CKAP5* mRNA and circZNF609 was performed using starBase 2.0 (Li et al., 2014) filtering for "CLIP_data>=1" and "programNum>=3."

QUANTIFICATION AND STATISTICAL ANALYSIS

The distribution and deviation of data shown in the figures of this work, the statistical tests used to calculate significant differences, and the exact value of n (e.g., number of biological replicates of the experiments) are denoted in figure legends. When possible, individual datapoints from biological replicates were depicted as dots in the graphs. In main figure legends SE stands for standard error and SD stands for standard deviation.

Significance values were depicted in the figures using the following key legend: *$p < 0.05$, **$p < 0.01$, ***$p < 0.001$, ****$p < 0.0001$. The exact p values of statistical confrontations shown in main figures are indicated in the corresponding figure legend.